Eidgenössische Technische Hochschule Zürich
Swiss Federal Institute of Technology Zurich

Bio-Inspired Robotics Lab
Prof. Dr. Fumiya Iida

Master-Thesis

Quantification of Preview Control Walking Pattern Generation by Center of Mass Tracking

of a Four-Link Inverted Pendulum

Autumn Term 2014

Supervised by:
Prof. Katie Byl at USCB
Prof. Fumya Iida at ETHZ

Author:
Sebastian Altwegg
altweggs@ethz.ch

Contents

Abstract **iii**

Acknowledgments **v**

Symbols **vii**

1 Preliminaries **1**
1.1 Introduction . . . 1
1.2 Zero-Moment Point and Stability Criterion . . . 2
1.3 Walking Trajectory Generation by Preview Control . . . 3

2 Cart-on-Table Model **7**
2.1 Model Description . . . 7
2.2 Cart-on-Table Controller . . . 9
2.2.1 LQR State Feedback Controller . . . 9
2.2.2 ZMP Limit Force Controller . . . 11
2.3 Results for Cart-on-Table Model . . . 13
2.3.1 Standing Case (Single Support) . . . 13
2.3.2 Walking Case . . . 14
2.3.3 Summary . . . 19

3 Four Link Robot **21**
3.1 Model Description . . . 21
3.2 Four-Link Controller . . . 23
3.2.1 Model-Based Feedforward Control (MFC) . . . 26
3.2.2 Ankle Torque Reduction (ATR) . . . 26
3.2.3 Model Predictive Control (MPC) . . . 27
3.3 Results for Four-Link Robot . . . 28
3.3.1 Tracking Quality . . . 29
3.3.2 Robustness . . . 31

4 Conclusion and Outlook **35**
4.1 Conclusion . . . 35
4.2 Outlook . . . 36

A Explicit LQR Basin of Attraction **37**

B Four-Link Model Equation of Motion **43**

C Impulse on Four-Link Model **45**

Abstract

This thesis quantifies the applicability of preview control walking pattern generation on a four-link inverted pendulum robot model by center of mass tracking. The introduction of a mapping function for the center of mass to reference angles allows the use of mode-based feedforward control with high feedback gains for precise center of mass tracking. This method however lacks in robustness which is increase by ankle torque reduction. To conclude the project, the results of the developed controller are compared with an online optimization approach.

Acknowledgments

I would like to thank Prof. Katie Byl for supervising my thesis in the robotics lab at the University of California, Santa Barbara. I greatly appreciated her support, creative ideas and inspiring inputs throughout the project. I would also like to thank Prof. Fumiya Iida from ETH Zurich for encouraging me and supporting my wish to write the Master thesis abroad. Last but not least I would like to thank my girlfriend Kelly Xu for always motivating me, Markus Giftthaler and Chakrit Bhamornsiri for all the inspiring lunch breaks at UCSB and my friends for providing an alternation to my work.

Symbols

Symbols

x, y, z	Cartesian coordinates
ξ	Zero moment point
F	Force
p	Impulse
L	Length of link
l_c	Distance from joint to center of mass of one link
m	Mass
J	Inertia around the center of mass
g	Gravitational constant ($9.81 \frac{m}{s^2}$)
K_p, K_d	Controller gains

Indices

x, y, z	x, y, z direction
lim	limit
pos, neg	positive, negative
ref	reference
des	desired
CoM	Center of Mass

Acronyms and Abbreviations

ETHZ	Eidgenössische Technische Hochschule Zürich
UCSB	University of California, Santa Barbara
ZMP	Zero Moment Point
CoM	Center of Mass
CoB	Center of Body
UB	Upper Body

GRF	Ground Reaction Force
BoA	Basin of Attraction
RoT	Region of Trust
SP	Support Polygon
MPC	Model Predictive Control
MFC	Model-Based Feedforward Control
ATR	Ankle Torque Reduction

Chapter 1

Preliminaries

1.1 Introduction

The idea of robots assisting humans in a broad range of situations, from daily life [7] to disaster-recovery missions [4], has driven research in humanoid robotics over the past few decades and has led through technological advances to sophisticated systems such as ASIMO [16], HRP-3 [11] and ATLAS [4]. To safely maneuver in a variety of environments without tipping over, real-time gait planning and walking control is required. In order to break down the complexity of this task, most approaches separate the generation of reference trajectory from stabilization around it.

Two different concepts of generating the walking trajectory are commonly used. The first approach requires precise knowledge of the robot dynamics and computes a walking trajectory based on the zero moment point of the humanoid. In [2] an optimal control approach is used to generate with a reference trajectory, the application of an optimal gradient based optimization provides a solution in [13] and nonlinear optimization is applied in [3] for trajectory generation. Those optimization based algorithms on complex robot models accurately represent the real system but involve high computational efforts.

To speed-up calculations, low dimensional humanoid models are used for the generation of trajectories in the second method. Variations of inverted pendulums are frequently used as models. Due to their simplicity, fast on-line trajectory generation can be achieved but stabilization of the complete robot much relies on feedback control. Examples include stable walking pattern generation by indirect manipulation of the ZMP in [18] or trajectory generation in 3D-space by using a linear inverted pendulum in [9]. One of the most successful approaches has been developed by Kajita in [8] where ZMP preview control of a linear inverted pendulum to allow arbitrary foot placement.

Various controllers for stabilization of the robot around the reference trajectory have been developed and only a few inspiring approaches are pointed out. A posture/force control method, such that the robot can be regarded as inverted pendulum and easily track the reference trajectory, is described in [10], ankle torque reduction control to increase robustness is used in [6] and a model predictive control approach for push recovery has been developed in [17].

To perform tasks for disaster relief missions in the ongoing DARPA robotics challenge [4], maneuvering through unstructured environment is required. This demands high robustness of the robot with respect to perturbations. Therefore, this thesis quantifies the capability of the preview control walking pattern generator described in [8] by applying center of mass tracking of a four-link

inverted pendulum in the sagittal plane. Introducing a mapping from the center of mass to relative angles four the four-link model, allows the application of model-based feedforward control with high feedback gains for stabilizing the system around the generated reference trajectory. The simplicity of suggested controller ensures real-time gait planning and walking control. To compare the introduced feedback controller, an optimization based solution is developed and taken as reference. The quantification of the walking control, including pattern generation and stabilizing feedback control, is organized as follows:
In Chapter 2, limitations of pattern generator are examined by developing stabilizing feedback control to track the planned trajectories for a cart-on-table model. A robustness analysis provides a basin of attraction for the states of the cart. Chapter 3 introduces a four-link robot model in the sagittal plane to examine the applicability of the generated walking pattern for higher order models. By applying model-based feedforward control, center of mass tracking is achieved. Additionally, An ankle torque reduction strategy is discussed to increase robustness. To quantify the quality of the controller is is compared with an optimization based solution. The thesis is concluded with a conclusion and some remarks about future steps in Chapter 4.

1.2 Zero-Moment Point and Stability Criterion

One of the main goals in humanoid walking is to maintain dynamic stability. Inspired by Vukobratovic's ZMP review in [19], this section introduces the concept of the zero moment point and explains its influence on the stability criterion that will be used throughout this thesis.
By ensuring that the foot's area is in full contact with the ground and not only the edge, dynamic stability can be achieved. The influence of the robot on the foots dynamics are captured in ankle torque τ_A and force F_A and are balanced out by the ground reaction torque τ_R and force F_R. Figure 1.1a provides an overview of all involved forces and torques. Assuming sufficiently large friction to avoid slipping between foot and ground, the horizontal components of the reaction force $F_{R,x}$, $F_{R,y}$ and the torque $\tau_{R,z}$ compensate for the corresponding ankle influences.

$$\tau_{A,z} = \tau_{R,z} \tag{1.1}$$

$$F_{A,x} = F_{R,x} \tag{1.2}$$

$$F_{A,y} = F_{R,y} \tag{1.3}$$

By varying the point of attack of the ground reaction within the support polygon, the torques of the ankle are compensated and allows the reaction torques to remain zero. However, in the limit case the ankle torque pushes the point of attack to the edge of the support polygon and any additional torque will cause a rotation of the foot. This leads to the definition of the zero moment point and the stability criterion:

Definition 1 *The zero moment point is the point on the floor where the torques $\tau_{R,x} = 0$ and $\tau_{R,y} = 0$. If this point exists within the supported polygon, the robot remains stable and no rotation around the edge of the foot occurs.*

It is important to mention that the notation of the ZMP only exists within the support polygon and therefore coincides with the center of pressure for dynamically stable gait. In the unstable case, there is no ZMP, the CoP is at the edge of the support polygon and the ankle torques causes a rotation around that point. Knowing that the verical component of the ground reaction force

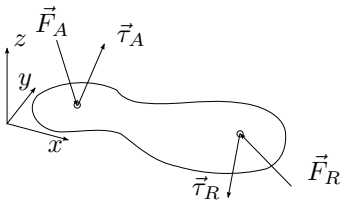

(a) Projection of one foot with all involved ankle and reaction fores and torques ankle.

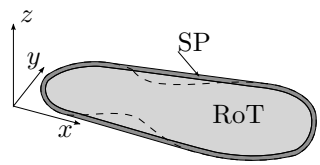

(b) Illustration of support polygon SP and trusted region RoT for the same foot projection.

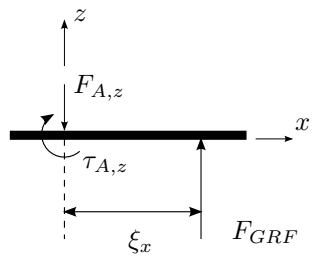

(c) Profile of the foot in the x-z-plane and all relevant forces and torques needed for the ZMP ξ_x calculations in x-direction.

Figure 1.1: Forces and torques acting on the foot in as displayed in 3D and in the sagittal plane.

compensates $F_{A,z}$ and following Definition 1, the equation for the ZMP is derived

$$\xi_x = \frac{\tau_{A,y}}{F_{R,z}} = \frac{\tau_{A,y}}{F_{A,z}} \tag{1.4}$$

$$\xi_y = -\frac{\tau_{A,x}}{F_{R,z}} = -\frac{\tau_{A,x}}{F_{A,z}} \tag{1.5}$$

where ξ_x and ξ_y are the positions of the ZMP on the support polygon. Figure 1.1c provides a side-view of the robots foot to support the understanding of this result.
To include for model uncertainties, a safety margin with respect to the full support polygon is introduced as shown in Figure 1.1b. This sets a limit on the ZMP in positive and negative direction

$$\xi_{neg} \leq \xi \leq \xi_{pos} \tag{1.6}$$

For ZMPs within this region of trust stability is guaranteed.

1.3 Walking Trajectory Generation by Preview Control

Trajectory generation by changing the food placement from their original assignment of an inverted pendulum as robot model has led to stable walking in [9]. In this sense, walking on surfaces where a deviation from the originally planned gait is not desired, the previously cited approach is not applicable. In [8], Kajita suggests a preview control approach to successfully prescribe precise foot placements. Since this method will be used throughout the thesis, some further information about the trajectory generator is provided in the following.

The equation of motion for the 3-D linear inverted pendulum with a constant height z_c of the point mass m is

$$\ddot{y} = \frac{g}{z_c} y - \frac{1}{m z_c} \tau_x \tag{1.7}$$

$$\ddot{x} = \frac{g}{z_c} x + \frac{1}{m z_c} \tau_y \tag{1.8}$$

where $x, y \in \mathbb{R}$ are the coordinates of the point mass m. Considering the equation of the ZMP

$$\xi_x = -\frac{\tau_x}{mg} \tag{1.9}$$

$$\xi_y = \frac{\tau_y}{mg} \tag{1.10}$$

and solving for the torques τ_x and τ_y, leads to the dynamic equation of motion of 3D pendulum as function of the ZMP position.

$$\xi_x = y - \frac{z_c}{g} \ddot{y} \tag{1.11}$$

$$\xi_y = x + \frac{z_c}{g} \ddot{x} \tag{1.12}$$

$$\tag{1.13}$$

Since the dynamics in x- and y-axis are decoupled, the two directions can be treated separately. To justify the introduction of the cart-on-table model in Chapter 2 it is important to mention, that the motion of a cart with mass m on a table with height z_c leads to the same dynamics.
The generation of the walking pattern is the inverse problem of the above: We want the control the motion of the cart such that the ZMP follows a certain trajectory which is determined by desired footholds. By only considering thesagittal plane, this problem can be formulated as a control task with system input u_x (see Figure 1.2).

$$\frac{d}{dt} \ddot{x} = u_x \tag{1.14}$$

and leads to the following linear system

$$\frac{d}{dt} \begin{pmatrix} x \\ \dot{x} \\ \ddot{x} \end{pmatrix} = \begin{pmatrix} 0 & 1 & 0 \\ 0 & 0 & 1 \\ 0 & 0 & 0 \end{pmatrix} \begin{pmatrix} x \\ \dot{x} \\ \ddot{x} \end{pmatrix} + \begin{pmatrix} 0 \\ 0 \\ 1 \end{pmatrix} u_x \tag{1.15}$$

$$\xi_x = \begin{pmatrix} 1 & 0 & z_c \end{pmatrix} \begin{pmatrix} x \\ \dot{x} \\ \ddot{x} \end{pmatrix} \tag{1.16}$$

While walking, the desire ZMP trajectory is a half cosine between the planned footholds. Based on the relationship between the CoM and the ZMP, the mass has to move before the ZMP step and therefore requires the use of a preview control algorithm. The design of the optimal preview controller follows the method of Katayama [12]. The system from the previously shown control task has to be discretized for a sampling time T

$$x_{k+1} = A x_k + B u_k \tag{1.17}$$

$$\xi_k = C x_k \tag{1.18}$$

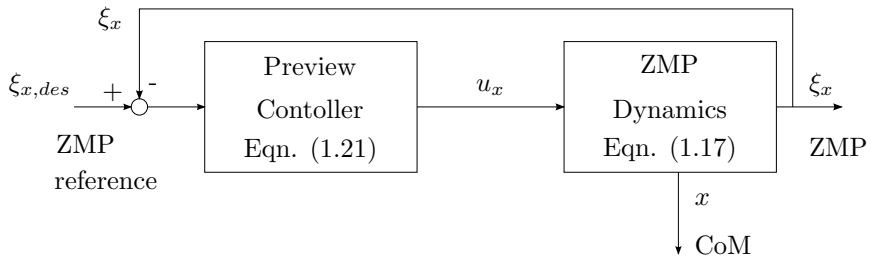

Figure 1.2: Structure for ZMP preview control developed by Kajita. A reference ZMP ξ and CoM x trajectory is generated on behalf of a desired ZMP ξ_{des} trajectory by applying preview control.

where $x_k = [x(kT), \dot{x}(kT), \dot{x}(kT)]^\top$, $u_k = u_x(kT)$ and $\xi_k = \xi_x(kT)$. A, B and C are the discretized system matrices.
The optimal control input is calculated such that the cost function

$$J = \sum_{i=k}^{\infty} \left\{ Q_e e_i^2 + \Delta x_i^\top Q_x x_i + R \Delta u_i^2 \right\} \tag{1.19}$$

is minimized as a function of the ZMP error $e_k = \xi_k^{des} - \xi_k$, the incremental state vector $\Delta x_k = x_k - x_{k-1}$ and the incremental input $\Delta u_k = u_k - u_{k-1}$. The matrices $R > 0$, Q_e and Q_x are the weights for the cost function J. The corresponding optimal controller is given by

$$u_k = -G_i \sum_{i=0}^{k} e_k - G_x x_k - \sum_{j=1}^{N_L} G_p(j) \xi_{k+j}^{des} \tag{1.20}$$

where N_L is the preview horizon and G_i, G_x and $G_p(j)$ are the gains obtained through the optimization in Equation (1.19) and the discretized system dynamics in Equation (1.15). Applying this preview control method provides a reference trajectory for the center of mass and the ZMP. In the following, stabilizing feedback controllers are introduced to achieve stable walking by center of mass reference tracking.

Chapter 2

Cart-on-Table Model

Based on a desired footholds and other step characteristics, Kajita's walking pattern generator provides a desired ZMP and CoM trajectory. This chapter quantifies the limits of this trajectory generation method by performing a robustness analysis on the same cart on a table model as used for the trajectory generator. The simplicity of the linear cart on a table model makes it easy to discuss stabilizing feedback control strategies for CoM reference tracking and to provide a robustness estimate for higher order models. As seen in Section 1.3 the motion in sagittal and frontal plane are decoupled and can be treated separately. Therefore, the complete controller design and robustness analysis is done in the sagittal plane only but it is assumed that the frontal plane can be treated the same way.

2.1 Model Description

Inspired by [8], Figure 2.1 shows the model in the saggital plane with parameters inspired by DARPA robotics challange robot ATLAS (see Table 2.1). For the derivation of the controllers and the robustness analysis the center of mass height is assumed to be at a constant height of $z_{CoM} = 0.8$ [m].
Having mentioned the relevant detail of the model allows one to derive the linear dynamics of the cart on the table and the corresponding ZMP.

$$\dot{\mathcal{X}} = A\mathcal{X} + B\mathcal{U} = \begin{pmatrix} 0 & 1 \\ 0 & 0 \end{pmatrix} \begin{pmatrix} \dot{x}_{CoM} \\ x_{CoM} \end{pmatrix} + \begin{pmatrix} 0 \\ \frac{1}{m} \end{pmatrix} F_x \tag{2.1}$$

$$\xi_x = C\mathcal{X} + D\mathcal{U} = \begin{pmatrix} 1 & 0 \end{pmatrix} \begin{pmatrix} \dot{x}_{CoM} \\ x_{CoM} \end{pmatrix} + \frac{-z_{CoM}}{m \cdot g} F_x \tag{2.2}$$

where the state $\mathcal{X}$ is the position and velocity of the cart and the input $\mathcal{U}$ is the force F_x acting on it in horizontal direction. By introducing a suitable feedback controller for the force, stabilization around the reference trajectories can be achieved. The testing of robustness will be done by applying a horizontal impulse p_x on the system. For simplicity, those impulses are transformed into velocities to provide a region of stable cart-on-table states. This collection of stable states is called basin of attraction (BoA) and allows instantaneous determination of stability. The conversion between

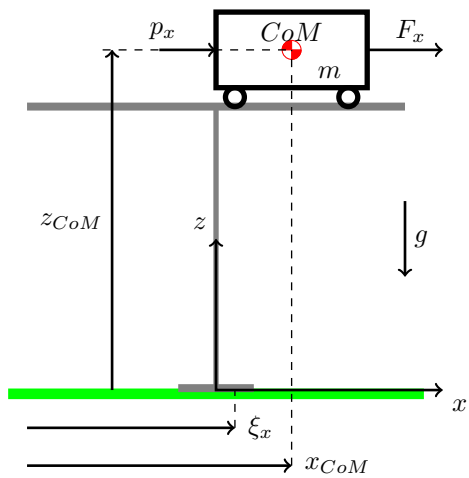

Figure 2.1: Model of the cart on a table used for the quantification of the preview control walking pattern generation on a low dimensional, linear model.

Parameter	Description	Value	Unit
z_{CoM}	constant height of CoM	0.8	m
m	mass of total robot	88.02	kg
SP_x	size of support polygon	$[-0.125 \ldots 0.125]$	m
-	desired safety margin	0.02	m
RoT	region of trust	$[-0.105 \ldots 0.105]$	m
g	gravitational constant	9.81	m/s^2

Table 2.1: Relevant model parameters ispired by the DARPA ATLAS robot dimensions [15].

impulses to velocities is straight-forward.

$$m \cdot \dot{x}^{+}_{CoM} = m \cdot \dot{x}^{-}_{CoM} + p_x \tag{2.3}$$

$$\dot{x}^{+}_{CoM} = \dot{x}^{-}_{CoM} + \frac{p_x}{m} \tag{2.4}$$

where $\dot{x}^{-}_{CoM}$ and $\dot{x}^{+}_{CoM}$ are the velocities of the cart before and after the impulse p_x.

2.2 Cart-on-Table Controller

For the stabilization of the cart around the reference trajectory, a combination of two controllers is suggested. A simple LQR state feedback controller is used to guarantee stabilizing behavior. The robustness is increased by the use of a bang-bang controller. Since this method computes an input force that sets the ZMP to the limit of the RoT it is called ZMP limit force controller. In the following, both approaches are described and an explicit BoA is derived to determine the robustness of the system.

2.2.1 LQR State Feedback Controller

To precisely track the x_{CoM} an LQR state feedback controller with a feedforward term containing the reference force, is introduced and leads to the system input

$$u(t) = K_p(x_{CoM,ref} - x_{CoM,act}) + K_d(\dot{x}_{CoM,ref} - \dot{x}_{CoM,act}) + m\ddot{x}_{CoM,ref} \tag{2.5}$$

where $[x_{CoM,act}, \dot{x}_{CoM,act}]$ indicate the current state of the cart and $\ddot{x}_{CoM,ref}$ is the acceleration of the cart derived by the second derivative of the CoM reference trajectory. Linearizing the system around the reference trajectory leads to the following system input

$$u(t) = -\begin{pmatrix} K_p & K_d \end{pmatrix} \begin{pmatrix} x_{CoM} \\ \dot{x}_{CoM} \end{pmatrix} \tag{2.6}$$

with x_{CoM}, $\dot{x}_{CoM}$ being the linearized states. Controlling the cart with this input leads to a second order system with corresponding ZMP.

$$\ddot{x}_{CoM} + \frac{K_d}{m}\dot{x}_{CoM} + \frac{K_p}{m}x_{CoM} = 0 \tag{2.7}$$

$$\xi_x = x_{CoM} - \frac{z_{CoM}}{g}\ddot{x}_{CoM} \tag{2.8}$$

The corresponding controller gains K_p and K_d derived through choosing the LQR cost matrices Q and R such that reasonable transient times are achieved while maintaining a certain robustness

$$R = 10^{-6}, \qquad Q = \begin{pmatrix} 1 & 0 \\ 0 & 10^{-5} \end{pmatrix} \tag{2.9}$$

The obtained LQR feedback gains K_p, K_d lead to an under-critically damped system of the form

$$x_{CoM}(t) = B \cdot \cos(\omega_d t + \eta) \cdot e^{-\zeta\omega_n t} \tag{2.10}$$

$$\text{with} \quad \omega_n = \sqrt{\frac{K_p}{m}}, \quad \zeta = \frac{K_d}{2\sqrt{K_p m}} \quad \text{and} \quad \omega_d = \omega_n\sqrt{1-\zeta^2} \tag{2.11}$$

The ZMP is calculated by plugging the explicit CoM solution into equation(2.8)

$$\xi_x = B\left(\underbrace{\left(1 + \frac{z_{CoM}}{g}\left(\omega_d^2 - (\zeta\omega_n)^2\right)\right)}_{K_1}\cos(\omega_d t + \eta) + \underbrace{\frac{z_{CoM}}{g}2\zeta\omega_n\omega_d}_{K_2}\sin(\omega_d t + \eta)\right)e^{-\zeta\omega_n t} \tag{2.12}$$

$$\xi_x = B\left(K_1\cos(\omega_d t + \eta) + K_2\sin(\omega_d t + \eta)\right)e^{-\zeta\omega_n t} \tag{2.13}$$

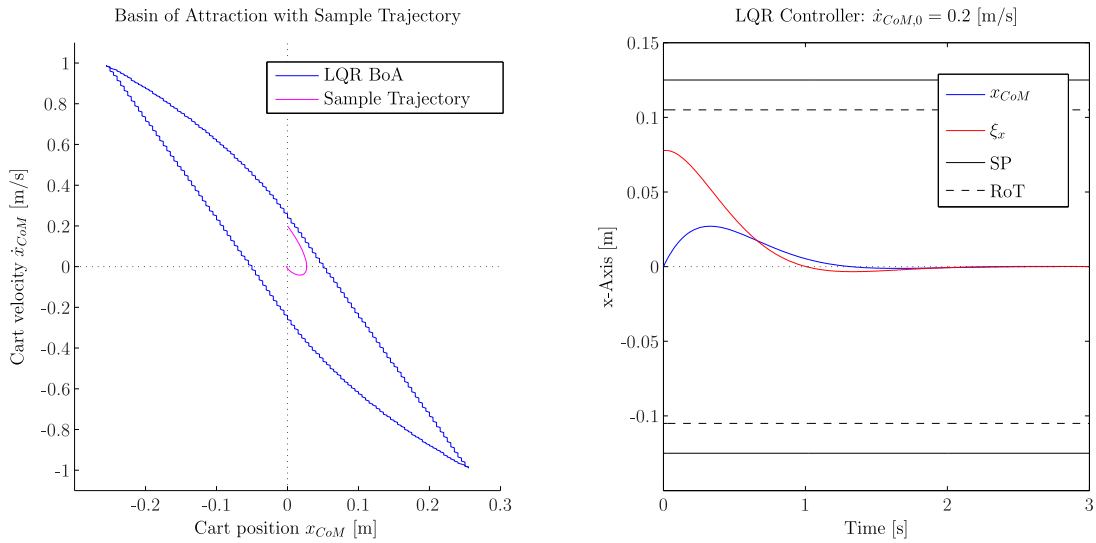

(a) Basin of attraction for the LQR controller as a function of the cart-on-table states x_{CoM} and $\dot{x}_{CoM}$. System remains stable for all states within the BoA.

(b) Behavior of the system under the influence of an impulse which leads to an inital velocity of 0.2 [m/s]. For stability, the ZMP must remain within the RoT.

Figure 2.2: Single support analysis of the LQR controlled system showing the basin of attraction in the state-space including the impulse response of the system, that is also shown in the time-domain.

Amplitude B and phase shift η are determined by the initial conditions $x_{CoM,0}$ and $\dot{x}_{CoM,0}$.

$$\dot{x}_{CoM}(t=0) = x_{CoM,0} = B\left(-\zeta\omega_n \cos(\eta) - \omega_d \sin(\eta)\right) \tag{2.14}$$

$$\Rightarrow B = \frac{1}{\omega_d}\sqrt{\dot{x}_{CoM,0}^2 + 2\dot{x}_{CoM,0} \cdot x_{CoM,0}\zeta\omega_n + x_{CoM,0}^2((\zeta\omega_n)^2 + \omega_d^2)} \tag{2.15}$$

$$x_{CoM}(t=0) = x_{CoM,0} = B \cdot \cos(\eta) \tag{2.16}$$

$$\Rightarrow \eta = \cos^{-1}\left(\frac{x_{CoM,0}}{B}\right) \tag{2.17}$$

Having stated the explicit equation of motion for the LQR controlled cart, an explicit basin of attraction can be derived which is done in Appendix A. The result of the BoA derivation is shown in Figure 2.2a. This allows instantaneous stability determination by checking whether the states are inside the BoA or not. This basin also provides information about the robustness of the system with respect to impulses by assuming they can be transformed into new cart states.

2.2.2 ZMP Limit Force Controller

For disturbances that lead to velocities outside the LQR basin of attraction, the system can not be stabilized anymore. With the introduction of a bang-bang controller this robustness is increased. The best possible method to recover from a large disturbance is to apply the largest counter-acting force that leads to a ZMP at the limit of the trusted region. This prevents the ZMP from leaving and provides the idea for naming this method ZMP limit force control. Setting the ZMP to the limit of the RoT $\xi_{x,lim}$ and reconsidering the dynamics of the cart, its equation of motion is derived

$$\xi_x(t) = \xi_{x,lim} = x_{CoM} - \frac{z_{CoM}}{g}\ddot{x}_{CoM} = \text{const.} \tag{2.18}$$

$$x_{CoM}(t) = C_1 e^{\sqrt{\frac{g}{z_{CoM}}}t} + C_2 e^{-\sqrt{\frac{g}{z_{CoM}}}t} + \xi_{x,lim} \tag{2.19}$$

$$\text{with} \quad C_1 = \frac{x_{CoM,0} - \xi_{x,lim}}{2} + \frac{\dot{x}_{CoM,0}}{2}\sqrt{\frac{z_{CoM}}{g}} \quad \text{and} \quad C_2 = \frac{x_{CoM,0} - \xi_{x,lim}}{2} - \frac{\dot{x}_{CoM,0}}{2}\sqrt{\frac{z_{CoM}}{g}} \tag{2.20}$$

where $x_{CoM,0} = x_{CoM}(t=0)$ and $\cot x_{CoM,0} = \dot{x}_{CoM}(t=0)$ are again the initial states of the cart. Through the construction of this control method, the ZMP is not capable of leaving the RoT. The originally introduced stability criterion has to be adjusted in the following way: The cart-on-table remains stable as long as the CoM trajectory does not leave the trusted region. By assuming that in the limit case, the CoM reaches its maximum at the edge of the RoT, the basin of attraction is derived

$$\frac{dx_{CoM}}{dt} = 0 = C_1\sqrt{\frac{g}{z_{CoM}}}e^{\sqrt{\frac{g}{z_{CoM}}}t_c} - C_2\sqrt{\frac{g}{z_{CoM}}}e^{-\sqrt{\frac{g}{z_{CoM}}}t_c} \tag{2.21}$$

$$t_c = \frac{1}{2}\sqrt{\frac{z_{CoM}}{g}}\log\left(\frac{C_2}{C_1}\right) \tag{2.22}$$

$$\frac{C_2}{C_1} > 0 \tag{2.23}$$

$$\dot{x}_{CoM,0} < \sqrt{\frac{g}{z_{CoM}}}(-x_{CoM,0} + \xi_{x,lim}) \tag{2.24}$$

Introducing positive $\xi_{x,pos}$ and negative $\xi_{x,neg}$ limits of the RoT the explicit solution for the basin of attraction is

$$\sqrt{\frac{g}{z_{CoM}}}(-x_{CoM} + \xi_{x,neg}) < \dot{x}_{CoM} < \sqrt{\frac{g}{z_{CoM}}}(-x_{CoM} + \xi_{x,pos}) \tag{2.25}$$

For all cart states within this BoA, the ZMP limit force controller is capable of preventing the CoM from leaving RoT. By looking at Figure 2.3 it is obvious that this controller as a stand-alone is not capable of stabilizing the system. However by combining this method with the previously described LQR controller, high robustness and stabilizing behavior is achieved. The use of the controller is determined by the corresponding basin of attraction as shown in Figure 2.4a. For states outside the ZMP limit force BoA, the system is unstable and will tip over if no recovery step is taken. The behavior of the cart in the time domain for a certain initial state is shown in Figure 2.4b.

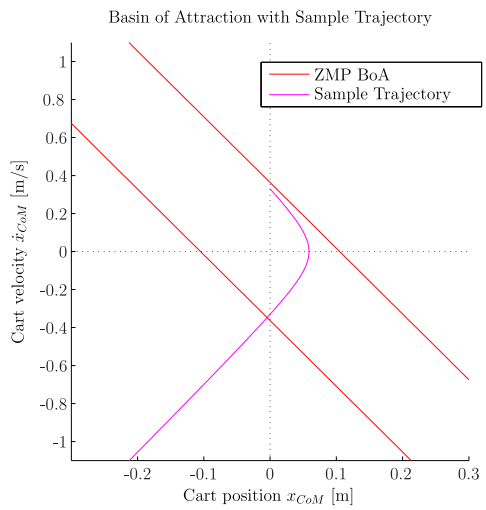

(a) Basin of attraction for the ZMP limit force controller as a function of the cart states x_{CoM} and $\dot{x}_{CoM}$.

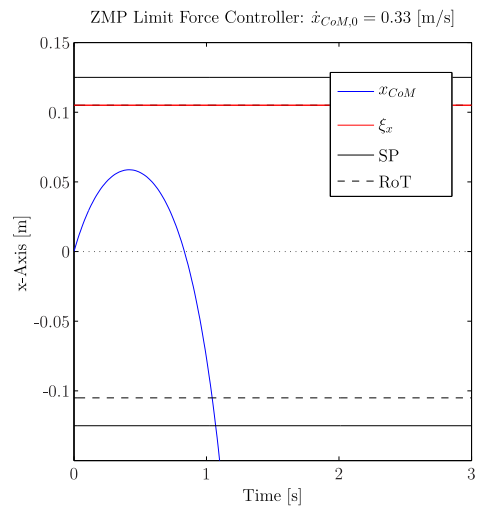

(b) Time-domain response of the ZMP limit force controlled system to an impulse that leads to an inital velocity of 0.33 [m/s].

Figure 2.3: Single support analysis of the ZMP limit force controlled system showing the basin of attraction in the state-space including the impulse response of the system the time-domain.

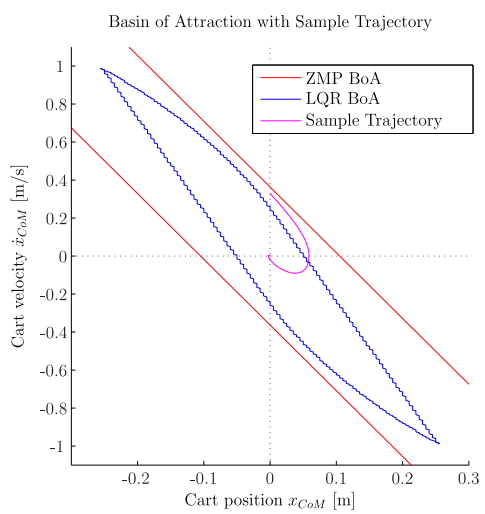

(a) Basin of attraction for the LQR/ZMP limit force combined controller as a function of the cart states x_{CoM} and $\dot{x}_{CoM}$.

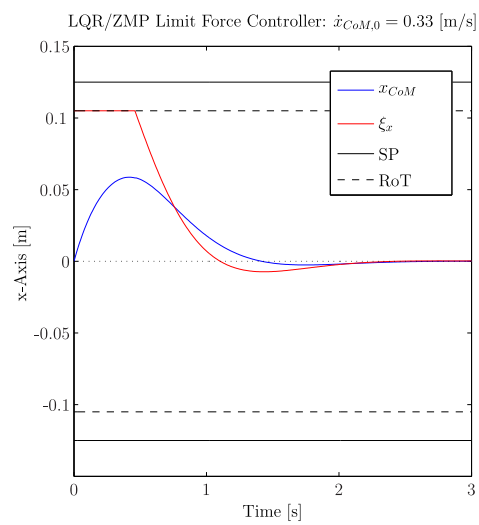

(b) Response of the LQR/ZMP limit force controlled system to an impulse that leads to an inital velocity of 0.33 [m/s].

Figure 2.4: Single support analysis of the LQR/ZMP limit force combined controlled system showing the basin of attraction in the state-space including the impulse response of the system in the time-domain.

2.3 Results for Cart-on-Table Model

The combination an LQR and ZMP limit force controller is found to be suitable to stabilize the cart on the table around its reference while increasing robustness. In the following, the robustness of the suggested controller in dependence of model and walking pattern variables is discussed for single support standing and walking case of the robot.

2.3.1 Standing Case (Single Support)

For the single support case the desired position of the ZMP and the CoM is at the center of the support polygon. The linearity and symmetry of the cart-on-table model allows one to predict that this configuration leads to the highest robustness. By looking at Equation (2.25) for the ZMP limit force BoA, it is clear that the limits of the robustness is a function of the CoM height z_{CoM} and the region of trust $p_{x,lim}$. Lower CoM heights lead to higher robustness since this causes a smaller angular momentum around the ankle. A larger support polygon allows to apply strong forces to counteract disturbances while maintaining stability and therefore increases the robustness too. The influences of both variables on the robustness is shown in Figure 2.5.

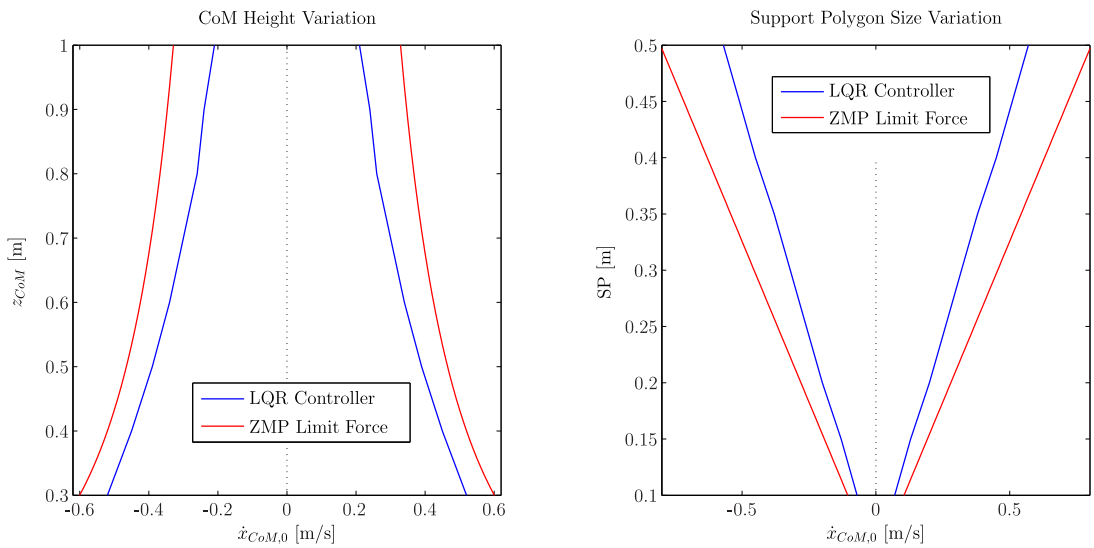

(a) Influence of the CoM height z_{CoM} on the robustness.

(b) Influence of the support polygon size SP on the robustness.

Figure 2.5: Influence of cart-on-table model parameters on the robustness of the system. The initial position of the cart is assumed to be at the center of the foot: $x_{CoM,0} = 0$ [m].

2.3.2 Walking Case

Humanoid gait characterization usually depends on a certain number of parameters. For the gait characterization of the cart-on-table model four distinct variables are used: Step size, total step time, time of the double support as fraction of the total step time and the height of the CoM. The choice of the step width is usually predetermined by desired footholds. Through the total step time a desired walking speed is induced. Based on those parameters a planned ZMP trajectory is suggested: As explained before, in the single support phase the ZMP is at the center of the RoT for high robustness in both, positive and negative, direction. During the double support phase, the ZMP between the desired footholds is connected by a half cosine. Based on this desired ZMP trajectory, Kajita's walking pattern generator provides a reference CoM and ZMP trajectory. Figure 2.6a shows the generated reference CoM and ZMP as well as the originally planed ZMP. To provide an overall statement on the robustness, the applied disturbances for the walking case correspond to the worst applicable single support disturbance.
In the remaining part of this section, the dependence of the robustness on the following gait and model parameters is examined: center of mass height z_{CoM}, stabilizing feedback controller, step size d_S, step time T_S and double support phase as fraction of total step time f_{DS}. The cart-on-table robustness is tested by applying the worst admissible single support disturbance at every time interval of 0.05 [s].

Feedback controller From the LQR basin of attraction we know that the robustness depends on the margin between the ZMP and the support polygon. To move the cart on the table from its initial position an acceleration is applied which causes a deviation of the ZMP from the desired position at the center of the RoT. This leads to a margin reduction and requires an adjustment of the LQR BoA to prevent the ZMP from leaving the RoT. Additionally, short double support times lead to an overshoot of the ZMP at each step and herewith to another margin reduction. Those qualities are shown in Figure 2.6a. Since the robustness mainly depends on the ZMP limit force BoA, a conservative assumption for the minimum LQR margin can be made without reducing the overall robustness. An analysis of the required margin for stability with respect to the double support fraction is made and shown in Figure 2.6b. The reduction of the RoT by 20% for the LQR controller is found suitable to maintain stability for different double support fractions.
The BoA of the ZMP limit force controller does not involve ZMP characteristics and is depending on the current state of cart only. Compared to the single support case, the CoM trajectory can leave the support polygon under the condition it re-enters again after making a step. The previously described BoA of the ZMP limit force controller remains unchanged for the double support case.
To summarize, the region of trust for the LQR controller and with it its BoA is artificially reduced to include for margin reductions cased by acceleration and deceleration of the cart. The boundaries of the RoT for ZMP limit force control remain unchanged. Therefore the same robustness as in the single support is achieved.

Center of mass height From the single support case we know that the robustness decreases with larger CoM heights. Since we are taking the same maximum disturbances as in the single support case the influence will be the same for walking. Another limitation induced by the CoM height is the maximum step width: Based on the geometry of the humanoid robot (see Chapter 3), the CoM height influence is examined for the range $z_{CoM} = [0.5 \ldots 0.9]$ [m] and limits the step width to $d_s \leq 0.5$ [m].

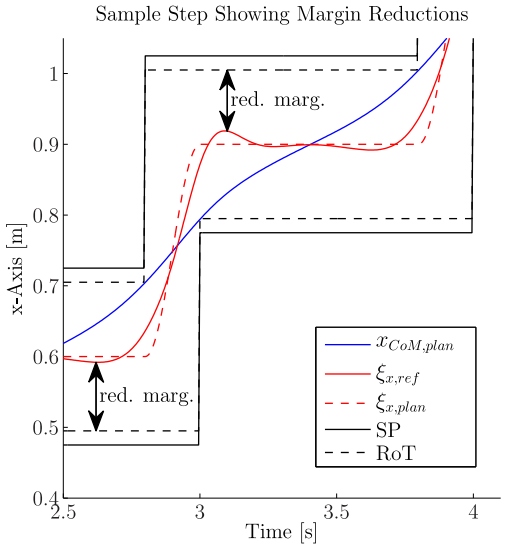

(a) Desired and planned ZMP and CoM trajectories and their influence on the margin reduction. For this walking pattern a double support fraction f_{DS} of 30% is chosen.

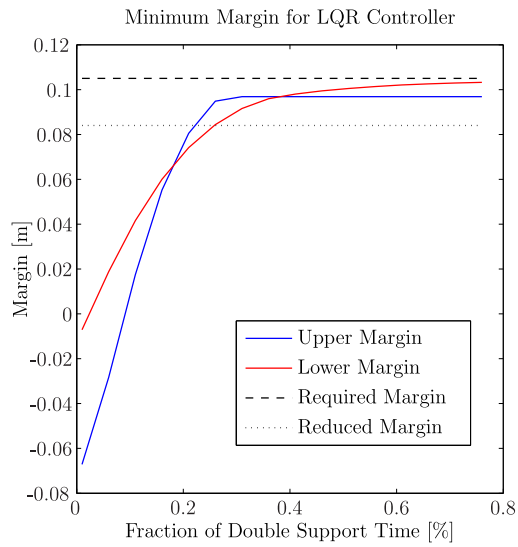

(b) Influence of the double support fraction f_{DS} on the margin between the ZMP and the RoT. A reduction of the trusted region by 20 % leads to a stable walking for $f_{DS} \geq 30\%$

Figure 2.6: Sample step and influences of the double support time on the margin between the ZMP and the RoT. For this analysis acceleration- and stopping step as described later are included and the following step characteristics are chosen: $z_{CoM} = 0.8$ [m], $d_S = 0.3$ [m] and $T_S = 1$ [s].

The robustness analysis for different CoM heights highlights the following result: For $z_{CoM} \leq 0.8$ [m] the step width up to 0.5 [m] are allowed. Height larger than this, $z_{CoM} > 0.8$, required a reduction to a maximum step width to 0.45 [m] to maintain stability for all configurations. Additionally, the lower the CoM height, the more double support time is needed to guarantee stable walking under the maximum suggested speed (see following paragraph). Figure 2.8 shows the just described qualities for the maximum and minimum considered CoM heights.

Total step time and step width These two variables determine the walking speed of the robot. Since the robot might have to follow a certain step pattern, the step width is predetermined and the remaining degree of freedom is the total step time. As a conclusion the limit is set on the walking speed rather than on the step time and width. Figure 2.7 shows the stability region as a function of the step time, step width for a constant double support time of 50 %. Assuming a minimum step time of 0.5 [s] and setting the maximum admissible CoM velocity to 2.5 [km/h] leads to a stable walking for all configurations. For higher CoM heights the velocity of the cart can be even higher up to 3.25 [km/h] if the maximum step width is limited to 0.45 [m]. This is just about in the range of other modern humanoid robots such as PETMAN (4.8 [km/h]) [14], ASIMO (1.6 [m/s]) [7] or HRP-3 (2 [m/s]) [1]. This observation might seem controversial to the statement made for the single support case, where larger CoM heights reduce the robustness. Since we are taking the worst single support disturbance for the corresponding height this has already been taken into

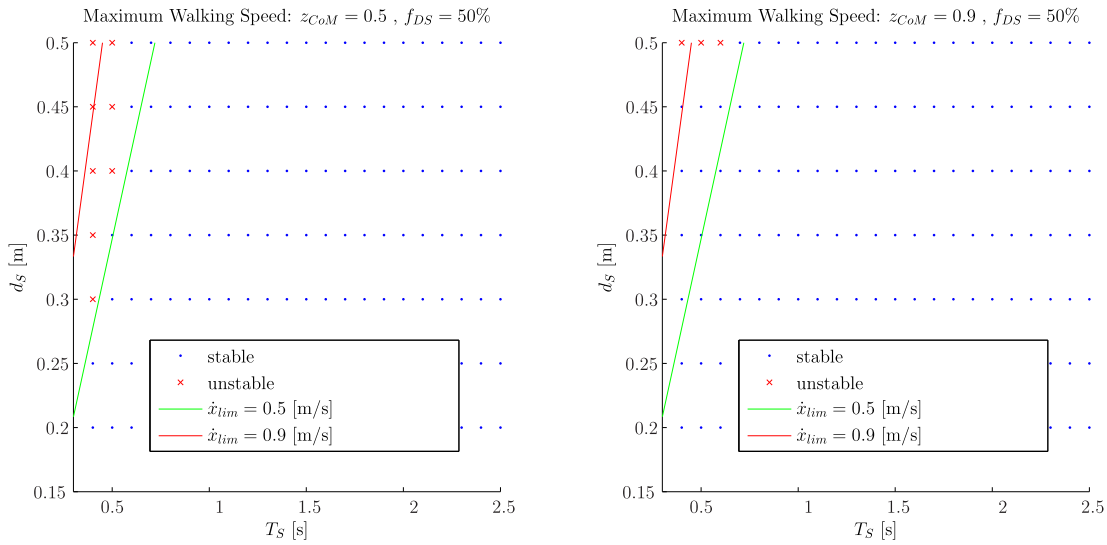

(a) Influence of step time and width on the stability for a CoM height of 0.5 [m].

(b) Influence of step time and width on the stability for a CoM height of 0.9 [m].

Figure 2.7: Comparison of the robustness for different CoM hights as a function of step width and step time, assuming a constant double support fraction of 50 %.

account. The herewith obtained variation of the impulse magnitude for different z_{CoM} leads to different ZMP trajectories that cause unstable walking for smaller CoM heights.

Double support phase The double support time, as a fraction of the total step time, defines the channel (see Figure 2.6) in which the ZMP has to transfer from one center of foot to the other. On one side, smaller channels require higher are accelerations and stopping forces and leads to an overshoot of the ZMP trajectory. This stability-critical margin reduction has been already taken care of by adjusting the trusted region of the LQR controller. In this sense, a long double support phase leads to higher robustness since less overshoot and a larger support polygon during that time can be achieved. On the other side, given a total step time, the double support phase also determines the time for swinging the leg. With regards to the four-link model in Chapter 3 high torques in the joints, used for fast swinging of the legs, influence the ZMP and with it the robustness of the robot and should therefore be avoided. As can be seen in Figure 2.8 the cart-on table model remains stable for most walking patterns and for all CoM heights for a range of double support fraction from 40% up to 80%. Suggesting a double support phase of 50 % allows enough time for the leg to swing to its new position and maintains the same robustness as the single support case.

Acceleration and stopping of planned gait The recovery from the largest acceptable disturbance in the single support case requires a certain time. Assuming one of these disturbances occurs at the beginning of a walking pattern with high desired CoM velocity, there might be not enough time to recover. Increasing step time of the first step solves this problem. The same observation is made at the last step before the cart-on-table comes to a stop: Walking with a high speed fol-

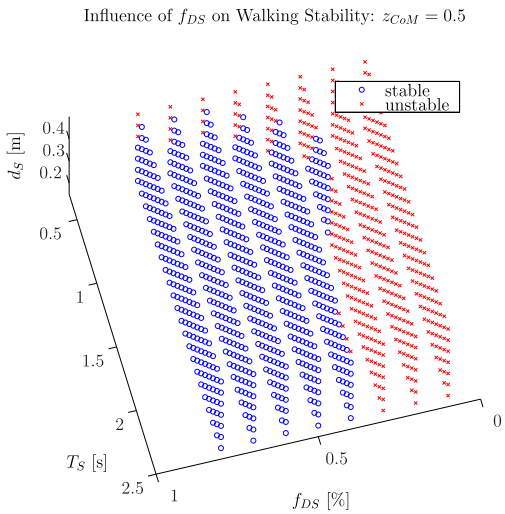

(a) Double support fraction influence on the robustness for a CoM height of 0.5 [m].

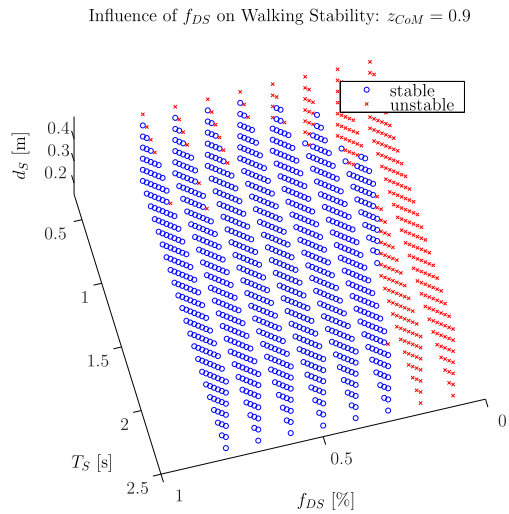

(b) Double support fraction influence on the robustness for a CoM height of 0.9 [m].

Figure 2.8: Results of the robustness analysis for the minimum and maximum CoM height: 30 % double support fraction leads to unstable walking for the height of 0.5 [m]. In comparison, for the height of 0.9 [m] this critical double support fraction is 20 %. To make sure that all configurations are stable a double support phase of 50 % is suggested.

lowed by a sudden stop leads to instability. As a method to avoid complications during walking, an acceleration and stopping step is suggested. Choosing an step time of 2.5 [s] for the first and last step of a certain walking pattern allows fast walking while maintaining stability. Simulations have shown that different fractions of double support phase at the start and end of the walking pattern lead to more stable configurations. Therefore an initial and final double support fraction of 50 % respectively 70 % is suggested. Influences of the acceleration and stopping step are shown in Figure 2.9. It also provides an overview on the robustness testing method: Applying the maximum admissible single support disturbance at every time interval of 0.05 [s] generates a new trajectory for the ZMP and CoM. By making sure that whether the ZMP exits the RoT and by making sure the CoM lies within the same boundaries at the end of the walking pattern, stability is determined.

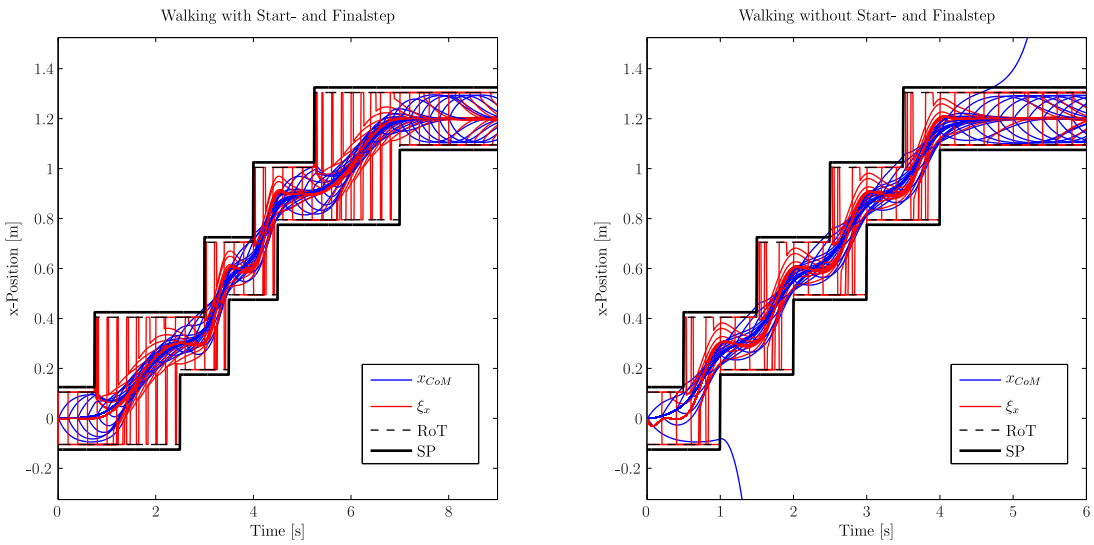

(a) Stable walking with initial and final step: CoM trajectory ends within the RoT and ZMP remains in the support polygon.

(b) No initial and final step leads to instability at both, start and end of the walking pattern: CoM leaves the support polygon.

Figure 2.9: Comparison of the robustness based on the same disturbance with and without initial and final step. Configuration: CoM height 0.5 [m], double support phase of 50 %, step width 0.3 [m] and step time 1 [s].

Parameter	Lower Bound	Upper Bound	Unit
Center of mass height z_{CoM}	0.5	0.9	[m]
Walking speed	-	2.5	[km/s]
Step width	-	0.45	[m]
Step time	0.5	-	[s]
Double support time	40	80	[%]

Table 2.2: Boundaries on the walking pattern variables to guaranteeleast single support robustness for the walking case of the cart-on-table model.

2.3.3 Summary

The robustness analysis of the single support provides a bound on the maximum admissible disturbance. To provide a lower bound on the robustness of the complete system (standing and walking), it is sufficient to show that walking leads to at least the same robustness. Therefore the worst admissible single support disturbance is applied to different walking patterns at every time interval of 0.05 [s]. Considering the limitations described in the Section 2.3.2 stable walking is achieved. The boundaries on model and walking pattern variables are summarized in Table 2.2. This table provides a conservative bound on the parameters: As long as the pattern and model variables stay between those boundaries, the walking case is at least as robust as the single support case. No statement about the maximum admissible disturbance is made but it is easy to show that for certain configurations of the walking pattern even higher disturbances can be handled by the cart-on-table.

Chapter 3

Four Link Robot

After having shown the influence of the preview control walking pattern generator on the simple cart-on-table model in Chapter 2, its applicability to higher order system is examined in this chapter. For this reason, a four-link inverted pendulum model is introduced in this chapter. By developing model-based feedforward control, CoM tracking of the reference trajectory is achieved. To increase the robustness of the system using this controller, an ankle torque reduction mode is added. The capabilities of this controller are shown, by comparing it with an optimization-based solution obtained through model predictive control.

3.1 Model Description

As shown in Figure 3.1a, the four-link model consists of shanks, thighs, torso and arms. The corresponding dimensions are derived from data of the DARPA challenge robot ATLAS and are summarized in Table 3.1. Using the relative angles of the four-link $q = [\theta_1 \theta_2 \theta_3 \theta_4]^\top$ as generalized coordinates and by applying Lagrangian's method, the dynamics of the robot model are derived (see Appendix B) and lead to the following generalized equation of motion

$$M(q)\ddot{q} + H(q, \dot{q}) = \vec{\tau} \tag{3.1}$$

where $M(q) \in \mathbb{R}^{4\times4}$ is the mass matrix of the system, $H(q, \dot{q}) \in \mathbb{R}^{4\times1}$ captures all Coriolis, centrifugal and gravitational forces and $\vec{\tau} = [\tau_1 \tau_2 \tau_3 \tau_4]^\top \in \mathbb{R}^{4\times1}$ contains the torques in the joint.
As described in Section 1.2, the stability of the four-link robot depends on the ankle torque τ_1 and ground reaction force F_{GRF}. For stability, the ZMP determined by those two values, must lie inside

No. i	Link	Mass [kg] m_i	Inertia [kg m^2] J_i	Length [m] L_i	Length CoM [m] lc_i
4	Arms	19.96	0.5935	0.645	0.3717
3	Torso	42.03	3.542	0.752	0.2536
2	Thighs	17.09	0.311	0.424	0.1984
1	Shranks	8.93	0.163	0.422	0.2297

Table 3.1: Parameters of the four-link robot inspired by the ATLAS robot [15].

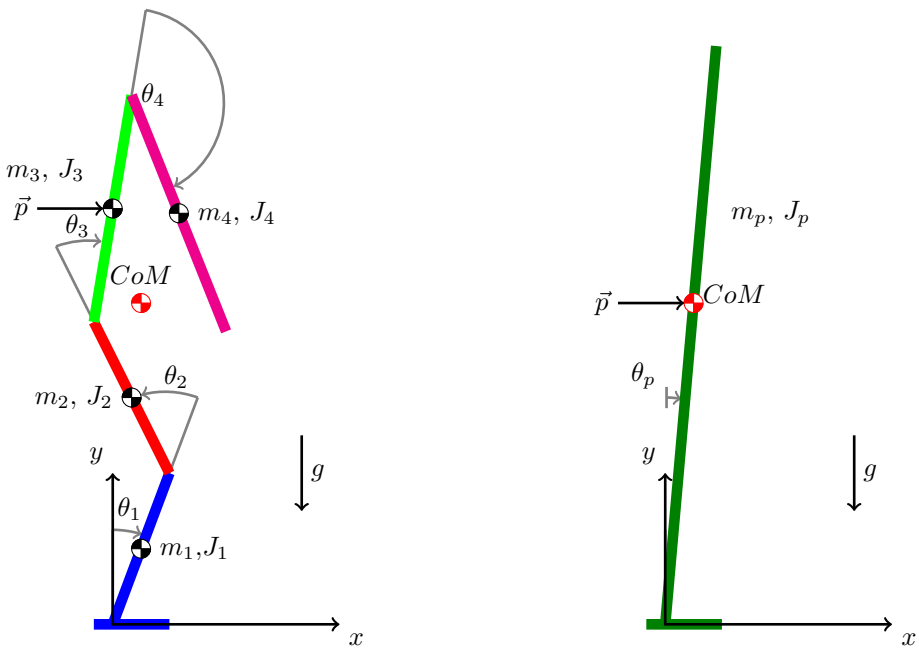

(a) Four-link model of the ATLAS robot in the sagittal plane.

(b) One-link inverted pendulum model obtained through locking four-link joints.

Figure 3.1: Simplified robot models inspired by the ATLAS robot in the sagittal plane. The one-link model is obtained by combining links of the four-link robot into one single link. This can be achieved by locking all relative joints or by applying high gain feedback control on all non-ankle joints.

the region of trust. Taking the complete foot as support polygon and introducing a safety margin of 1 [cm] from the heel respectively 2 [cm] from the toes, leads to a RoT of $[-0.04 \ldots 0.18]$ [m]. This limiting factor provides a bound on the ankle torque

$$F_{GRF} \cdot \xi_{x,neg} \leq \tau_1 \leq F_{GRF} \cdot \xi_{x,pos} \tag{3.2}$$

$$\text{with} \quad F_{GRF} = m_{tot} \left(g - \ddot{y}_{CoM}\right) \tag{3.3}$$

where m_{tot} is the total mass of the robot and $\ddot{y}_{CoM}$ the acceleration of the CoM in y-direction. $\xi_{x,neg}$ and $\xi_{x,pos}$ are the negative and positive limits of the ZMP induced by the RoT. The F_{GRF} is only the vertical component of the ground reaction force.
In addition to the four-link model, a single link inverted pendulum is introduced (see Figure 3.1b). This model is easy to analyze and closely related to the cart-on-table from the previous chapter. The one-link model can be achieved by either using controllers with high feedback gains on all joints but the ankle or by locking the same joints. The upper part of the robot is kept at its desired position and the model can be treated as single-link inverted pendulum. Since the stability of the system depends on the ankle torque and the vertical acceleration of the CoM only, a separate controller for the ankle can be used to stabilize to complete four-link robot, that behaves like a one-link inverted pendulum. Introducing this model allows easy separation of the upper body joint from the ankle. This decoupling is a helpful method to increase robustness of the system and will be explained in more details in Section 3.2.2. The equation of motion for one link with the ankle angle $\theta_p \in \mathbb{R}$ as generalized coordinate is

$$\ddot{\theta}_p \left(l_{cp}^2 m_p + J_p\right) - m_p \cdot g \cdot l_{cp} \sin\left(\theta_p\right) = \tau_p \tag{3.4}$$

where m_p is the total mass of the pendulum, J_p the total inertia of the four-link around the CoM and τ_p the ankle torque.

3.2 Four-Link Controller

The trajectory generator provides reference paths for the CoM and the ZMP as a function of time. Since the inputs to the system are the torques action on each joint, it is simple to control each angle separately but hard predict its influence on the CoM. By introducing a mapping function from the CoM to the relative angles this problem is avoided. The remaining task is to track the angles obtained as a function $\vec{f}$ of the reference CoM trajectory.

$$q_{ref}(t) = \vec{f}\left(x_{CoM,ref}(t), y_{CoM,ref}(t)\right) \tag{3.5}$$

$$\dot{q}_{ref} = \frac{d}{dt} q_{ref} \quad \text{and} \quad \ddot{q}_{ref} = \frac{d^2}{dt^2} q_{ref} \tag{3.6}$$

The CoM positions x_{CoM} and y_{CoM} provide two constraints that are used for the mapping function. To complete the mapping, the introduction of two additional constraints is necessary. This is done by prescribing different limit poses which lead to desired arm and torso trajectories. The following two cases for limit poses are examined:

- Steady arm and body link in the sense of absolute joint angles. Legs are responsible for CoM transition, torso and arms are constant for all x_{CoM}.

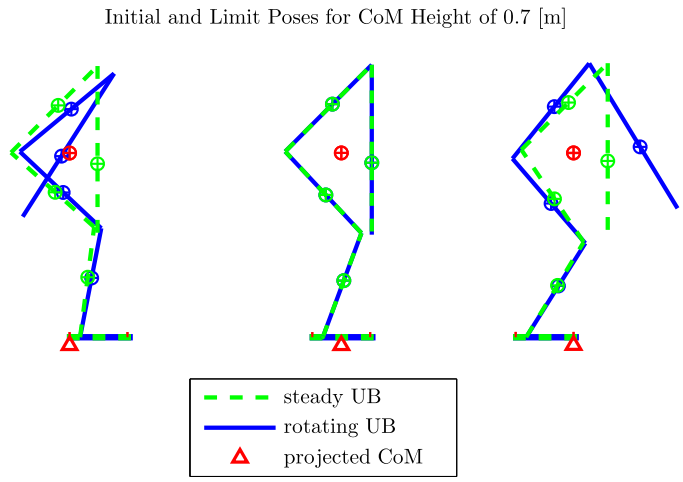

Figure 3.2: Poses used for mapping of the CoM position to angles. Inital pose is energy optimized and leads to a CoM in the center of RoT. Limit poses are following the above constraints and show a CoM above the edge of the support polygon.

- Counter rotation of the upper body to compensate for angular momentum caused by the lower body. Relative arm and torso angles are a function of x_{CoM}.

Starting from an energy optimized reference pose with a projected x_{CoM} at the center of the RoT, limit poses are derived by following the above described considerations. In a limit pose, the projected CoM x_{CoM} coincides with the limit of the trusted region. Figure 3.2 provides an overview of those poses for a constant CoM height $y_{CoM} = 0.7$ [m] which is taken as a basis for all further analysis. Fitting the angles of the limit and initial poses with a second order function leads to the desired mapping function that is illustrated in Figure 3.3a. As assumed for the preview control trajectory generator and the cart-on-table model, by applying these mapping functions the height of the CoM is kept at a constant height which is shown in Figure 3.3b). The remaining task is now to develop a suitable feedback controller for angular tracking and will be done in the following section. Figure 3.4 provides an overview of the complete control structure, showing the connection between the reference trajectory generator, mapping function, four-link controller and the robot model.

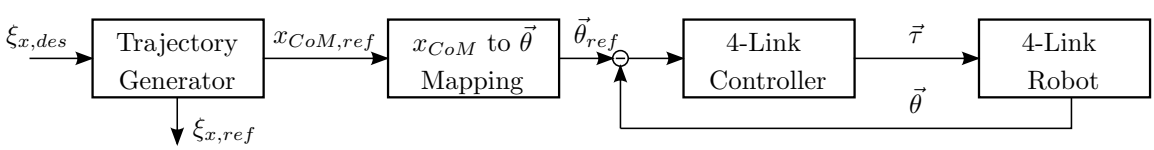

Figure 3.4: Control structure for the four-link robot model, showing the influence of the trajectory generator and mapping fuction.

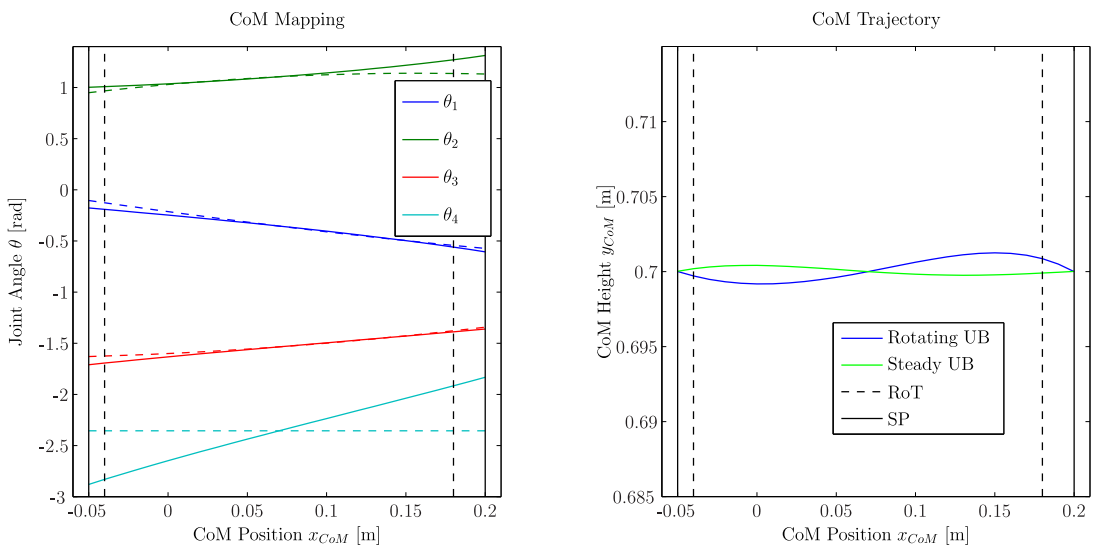

(a) Mapping function assigns relative angles for each joint as a function of x_{CoM} for both, constant (dashed lines) and rotating (solid lines) upper body.

(b) CoM height as a function of its position resulting from the different mapping function. Constant hight is desired to obtain similar behaviour as for the cart-on-table model.

Figure 3.3: Mapping function for reference CoM x_{CoM} position to reference angles $\vec{\theta}_{ref}$ and its influence on the CoM heigth y_{CoM}.,

3.2.1 Model-Based Feedforward Control (MFC)

The previously described relationship between the CoM and the angles of the four-link provides a reference trajectory over time for each link. Angular velocity and acceleration are calculated by taking the derivative of the obtained trajectories. Using information of the four-link model allows the estimation of the required torques to follow those trajectories. To allow precise tracking and to include for model uncertainties and errors, feedforward control is not sufficient and additional high-gain feedback is applied on each link

$$\ddot{q} = \ddot{q}_{ref} + K_p \left(q_{ref} - q\right) + K_d \left(\dot{q}_{ref} - \dot{q}\right) \tag{3.7}$$

$$\vec{\tau} = M \left(\ddot{q}_{ref} + K_p \left(q_{ref} - q\right) + K_d \left(\dot{q}_{ref} - \dot{q}\right)\right) + H \tag{3.8}$$

K_p and K_d are calculated based on desired angular error dynamics and leads to the following gains

$$K_p = 255 \cdot \mathbb{1}^{4\times 4} \quad \text{and} \quad K_d = 18 \cdot \mathbb{1}^{4\times 4} \tag{3.9}$$

where $\mathbb{1}$ is the unity matrix. These high gains of the controller lead to large torques for angular errors. As later explained in Section 3.3.2, applying an impulse on the system leads to a sudden change in angular velocities and therefore high velocity errors. The generated torques in the ankle, caused by high gain feedback control, are too large and cause the robot to tip over. By separately controlling the ankle torque this problem can be avoided and leads to the introduction of the ankle torque reduction controller.

3.2.2 Ankle Torque Reduction (ATR)

If zero ankle torque is assumed the stability of the robot depends on the location of the CoM only and torques in the remaining joints do not influence the stability directly. This leads to the introduction of the ankle torque reduction. Compared to the method developed in [6], where the ankle torque is reduced by a factor depending on the joints acceleration, this thesis assumes no ankle torque for a certain period.
For disturbances that are too large to handle for the MFC controller, the ankle torque is reduced to zero for a time of $t < t_{crit}$. As a result of simulations, this critical time is set to 0.03 [s]. Meanwhile, errors in angular position and velocity in all but ankle joints are corrected by the same high gain feedback controller as used in MFC. The four-link robot now behaves like a single link inverted pendulum. In a second step, after that critical time, the ankle of the one-link pendulum is controlled by using a combined strategy of ZMP limit torque and PD control, inspired by the cart-on-table model.

$$\tau_1 = \begin{cases} 0 \quad \text{for } t \leq t_{crit} \\ \left(J_p + m_p lc_p^2\right)\left(\ddot{\theta}_{p,ref} + K_{p,1}\left(\theta_{p,ref} - \theta_p\right) + K_{d,1}\left(\dot{\theta}_{p,ref} - \dot{\theta}_p\right)\right) - g m_p lc_p \sin\left(\theta_p\right) \\ \quad \text{for } t > t_{crit} \text{ and } \theta_p \in BoA_{PD} \\ \left(\frac{1}{m_p} - \xi_{x,lim}\frac{lc\sin\left(\theta_p\right)}{J_p + m_p lc_p}\right)^{-1}\left(g + lc_p\dot{\theta}_p^2\cos\left(\theta_p\right) + lc_p^2\sin^2\left(\theta_p\right)\frac{g m_p}{J_p + m_p lc_p^2}\right)\xi_{x,lim} \\ \quad \text{for } t > t_{crit} \text{ and } \theta_p \in BoA_{ZMP} \end{cases} \tag{3.10}$$

(3.11)

where $K_{p,1} = 9$, $K_{d,1} = 3.6$ are small gains for the PD control of the inverted pendulum and m_p, J_p, lc_p are the new one-link inverted pendulum parameters obtained through the lumped four-link model. The angles $\theta_p, \theta_{p,ref}$ are obtained from the corresponding four-link angle $\theta_1, \theta_{1,ref}$

by adding a constant offset. The remaining torques $[\tau_2 \dots \tau_4]$ are controlled with the previously described MFC controller.
The switching between ZMP limit and PD two controllers is based on a basin of attraction for the PD controller as a function of the ankle angle θ_p and total angular momentum $\dot{\theta}_p(J_p + m_p l c_p^2)$.

3.2.3 Model Predictive Control (MPC)

The idea behind MPC is to predict the dynamics of a system over a finite time horizon and calculated and optimal input based on a cost function. This optimization is repeated in each time-step T_s and provides torque inputs for the period of time horizon. One of the benefits of this method is the possibility to include constraints to the optimization process. Applied to our four-link model, this allows us to set limits on the ZMP. To efficiently compute optimal torques, the system dynamics, constraints, and cost function have to be transformed into a quadratic program.
First, the nonlinear four-link model needs to be linearized around its current state and the corresponding static torque.

$$\dot{x} = Ax + Bu + h \tag{3.12}$$

$$\text{where} \quad x = \begin{bmatrix} q \\ \dot{q} \end{bmatrix} \in \mathbb{R}^{8\times 1} \quad \text{and} \quad u = \begin{bmatrix} \tau_1 \\ \tau_2 \\ \tau_3 \\ \tau_4 \end{bmatrix} \in \mathbb{R}^{4\times 1} \tag{3.13}$$

with system matrices $A \in \mathbb{R}^{8\times 8}$, $B \in \mathbb{R}^{8\times 4}$ and $h \in \mathbb{R}^{8\times 1}$ to compensate for steady-state offset introduced through the linearization. To include for limitation on torques (see equation 3.3) the CoM acceleration in y-direction is linearized as well

$$\ddot{y}_{CoM} = Sx + Tu \tag{3.14}$$

where $S \in \mathbb{R}^{1\times 8}$ and $T \in \mathbb{R}^{1\times 4}$. Plugging the linearized CoM acceleration back into equation 3.3 provides a linear limit for the ankle torque

$$\tau_1 \leq m_{tot}(g - (Sx + Tu))\xi_{x,pos} \tag{3.15}$$

$$-\tau_1 \leq -m_{tot}(g - (Sx + Tu))\xi_{x,neg} \tag{3.16}$$

After discretizing the linear system and CoM acceleration the general form of the reference tracking MPC problem can be stated.

$$V(x) = \min_u \sum_{k=0}^{N-1} (x_k - x_{ref})^\top Q (x_k - x_{ref}) + (u_k - u_{ref})^\top R (u_k - u_{ref}) \tag{3.17}$$

$$\text{s.t.} \quad x_{k+1} = A_k x_k + B_k u_k + g_k, \quad x_0 = x \tag{3.18}$$

$$x_k \in \mathbb{X}, \quad u_k \in \mathbb{U} \quad \forall k \in \{0, \dots, N-1\} \tag{3.19}$$

where $Q \in \mathbb{R}^{8\times 8}$ and $R \in \mathbb{R}^{4\times 4}$ are the weighting matrices for the cost function $V(x) \in \mathbb{R}$ for the time horizon of N steps. The steady state targets x_{ref} and u_{ref} which the desired reference position at that time and the corresponding steady state torque. This notation is vectorized by introducing

the new coordinate $z = [x_0, u_0, x_1, u_1, \ldots, x_{N-1}, u_{N-1}, x_N]^\top$ and leads to a quadratic program with equality and inequality constraints

$$\min_z z^\top H z + f^\top z \tag{3.20}$$

$$\text{s.t.} \quad \mathcal{A} z = \mathcal{B} \tag{3.21}$$

$$\mathcal{C} z \leq \mathcal{D} \tag{3.22}$$

$$z \in \mathbb{Z} \tag{3.23}$$

with $H = \text{diag}[Q, R, \ldots Q_N]$ and $f^\top = -2[Qx_{ref}, Ru_{ref}, \ldots, Q_N x_{ref}]$ and the remaining matrices

$$\mathcal{A} = \begin{bmatrix} \mathbb{1} & 0 & 0 & 0 \\ A_0, B_0 & -\mathbb{1} & 0 & 0 \\ 0 & A_1, B_1 & -\mathbb{1} & \\ 0 & 0 & \ddots & \ddots \end{bmatrix}, \quad \mathcal{B} = \begin{bmatrix} x_0 \\ -h_0 \\ -h_1 \\ \vdots \end{bmatrix} \tag{3.24}$$

$$\mathcal{C} = \begin{bmatrix} -S_0 p_{x,pos} & -T_0 p_{x,pos} + \eta & 0 & 0 & 0 \\ S_0 p_{x,neg} & T_0 p_{x,neg} - \eta & 0 & 0 & 0 \\ 0 & 0 & -S_1 p_{x,pos} & -T_1 p_{x,pos} + \eta & 0 \\ 0 & 0 & S_1 p_{x,neg} & T_1 p_{x,neg} - \eta & 0 \\ 0 & 0 & 0 & 0 & \ddots \end{bmatrix}, \quad \mathcal{D} = \begin{bmatrix} g \cdot p_{x,pos} \\ -g \cdot p_{x.neg} \\ g \cdot p_{x,pos} \\ -g \cdot p_{x.neg} \\ \vdots \end{bmatrix} \tag{3.25}$$

where $\eta = [\frac{1}{M_{tot}}, 0, 0, 0]$. By using *quadprog*, the quadratic program solver provided by MATLAB's optimization toolbox, the optimization is solved at every time step T_s for a horizon of N steps and provides the optimal control input. This controller is now used to track reference trajectories for the angles $q_{ref}(t)$ and angular velocity $\dot{q}_{ref}(t)$ which are combined in x_{ref}. The corresponding optimized torques are obtained through the solution z. For the following analysis a prediction horizon $N = 15$ and a sampling time of $T_s = 0.02$ [s] are chosen.
To conclude the derivation of this controller a few important remarks concerning MPC are stated: Since an optimization has to be solved at each time interval T_s for the defined time horizon of N steps makes this method computationally excessive and real-time applicability is questionable. Also, since the control input is calculated based on a linear model and linearized constraints, the nonlinear ZMP could still violate the RoT boundaries.

3.3 Results for Four-Link Robot

The previous sections introduced all necessary tools to control the four-link inverted pendulum model. A reference trajectory is provided by using a preview control walking pattern generator. The obtained CoM trajectory is translated into reference angles that have to be tracked by the just described controllers. The remaining task is to quantify this walking control approach by discussing the tracking quality and robustness of the complete system. In addition to that, the influence of the introduced mapping function is discussed.

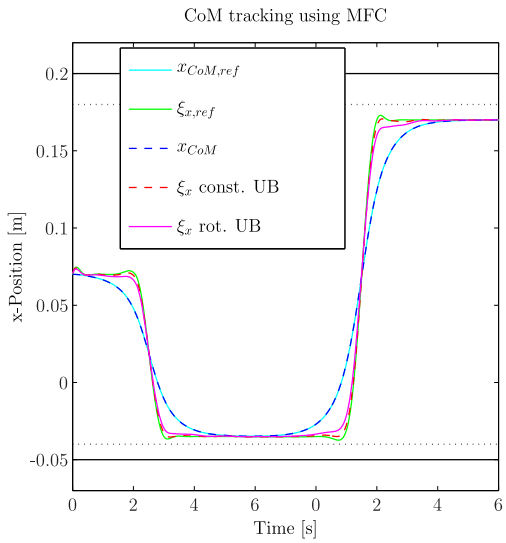

(a) CoM trajectory tracking by using MFC comparing constant and rotating upper body mapping function.

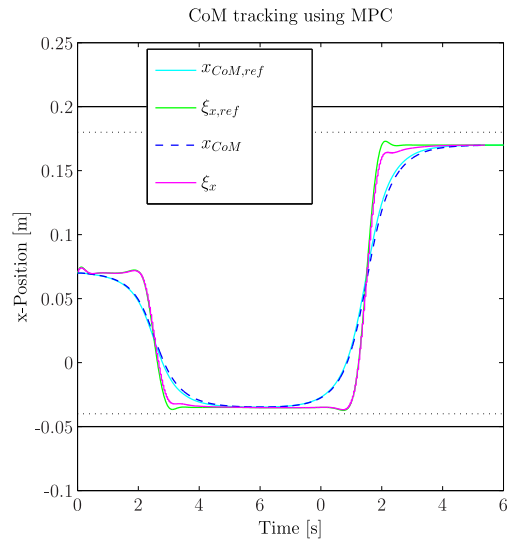

(b) CoM trajectory tracking using MPC and using the upper body counter rotation mapping function.

Figure 3.5: Comparison of tracking quality of MFC and MPC for a reference path obtained by Kajita's trajectory generator. The desired ZMP trajectory is chosen such that it remains within the RoT of the single support case.

3.3.1 Tracking Quality

The tracking quality of MPC and MFC is tested on a reference trajectory produced with Kajita's walking pattern generator. As mentioned before, the two methods do not directly control the ZMP but only CoM by using the described mapping function. The question is now, whether the actual ZMP follows the reference ZMP closely and stability can be guaranteed. This would also provide information on whether the relevant dynamics of the higher order four-link model are captured in the cart-on-table or not.

The desired ZMP trajectory for the pattern generator is chosen such that it imitates a step within the support polygon. Figure 3.5a and Figure 3.5b show the tracking behavior of the MFC and MPC controlled system for the same CoM reference trajectory. As can be seen, both controllers are capable of tracking the CoM precisely and lead to a ZMP that is following its predicted trajectory closely while maintaining stability. Considering the fact, that for the given problem, the MPC controller leads to a tracking error that is three times larger than the one of the MFC controller, there is no reason so far of using the computationally expensive MPC approach.

Considering the observation that the ZMP closely follows its predicted trajectory, it is assumed that the cart-on-table model captures the relevant dynamics of the higher order four-link model. This behavior mainly origins in the definition of the mapping function which influences two fundamental qualities. First, the defined mapping function leads to CoM heights that are roughly constant for all x_{CoM} positions and therefore closely imitate the cart-on-table model. Secondly, the transition of the CoM causes a rotation of all joints and therefore induces an angular momentum around the

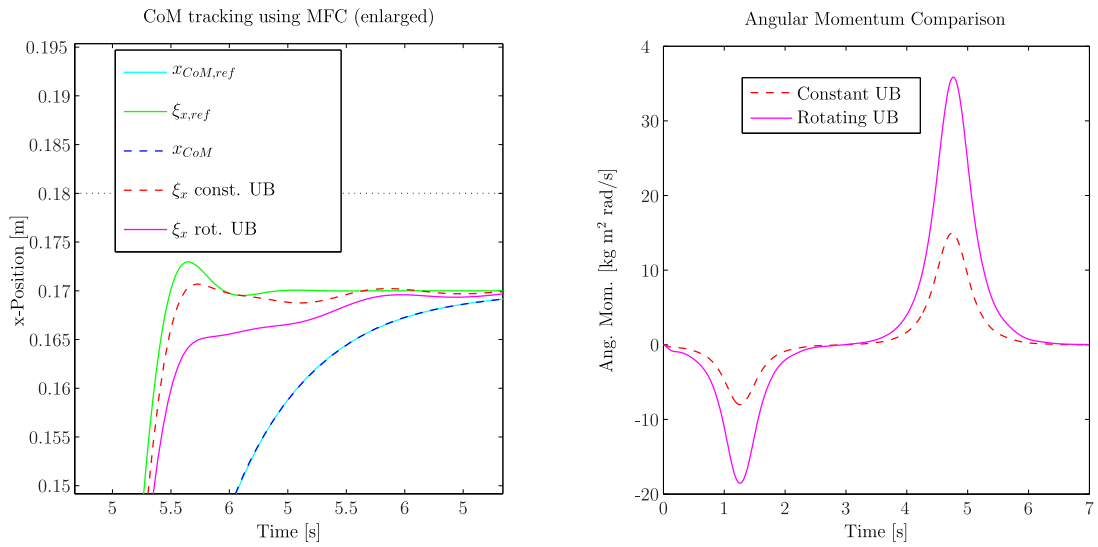

(a) Enlarged area of Figure 3.5a to highlight the influence of the mapping function.

(b) Angular momentum around the ankle for the different mapping functions.

Figure 3.6: Influence of the mapping function on the ZMP and the total angular momentum around the ankle: Counter rotation prevents peaks of the ZMP.

ankle joint. The introduction of limit poses that induce a counter rotation of the upper body, leads to an angular momentum that counteracts the CoM transition. As a result, smaller ankle torques are needed for stopping and acceleration of the CoM and therefore prevent robustness-reducing peaks of the ZMP. This quality is shown in Figure 3.6a where the discussed area is enlarged. The corresponding angular momentum around the ankle are provided in Figure 3.6b. Counter rotation of the upper body causes larger "counter angular momentum" and requires smaller torques in the ankle. As a result, smaller ZMP peaks are achieved.

The statement of the cart-on-table representing the higher order dynamics of the four-link system is further analyzed by deriving a basin of attraction for the four-link CoM position and velocity. From the cart-on-table analysis in Chapter 2 the CoM trajectory for any initial state is known. Tracking this trajectory as a reference and checking stability provides a BoA for the four-link CoM states. As a logical conclusion to taking the cart CoM as a reference, the controlled system it is hardly possible to achieve a larger BoA than the cart-on-table model. To avoid large errors in angular position and velocity, their initial state is set to coincide with mapped CoM initial state.

In Figure 3.7a the application of the reference trajectory is illustrated for a specific initial position and velocity of the CoM. Figure 3.7b shows the obtained basin of attraction for MFC as well as for MPC. The comparison of the four-link BoA under the influence of both controllers with the one of the cart-on-table for the same CoM height shows that they coincide within the RoT. For CoM positions outside the RoT, the BoA of the four-link controllers is smaller. This is related to kinematic constraints induced by mapping function. Those constraints lead to errors in the angles and therefore to high ankle torques and drive the system unstable.

As a summary of the tracking quality analysis it can be stated that precise CoM tracking can be

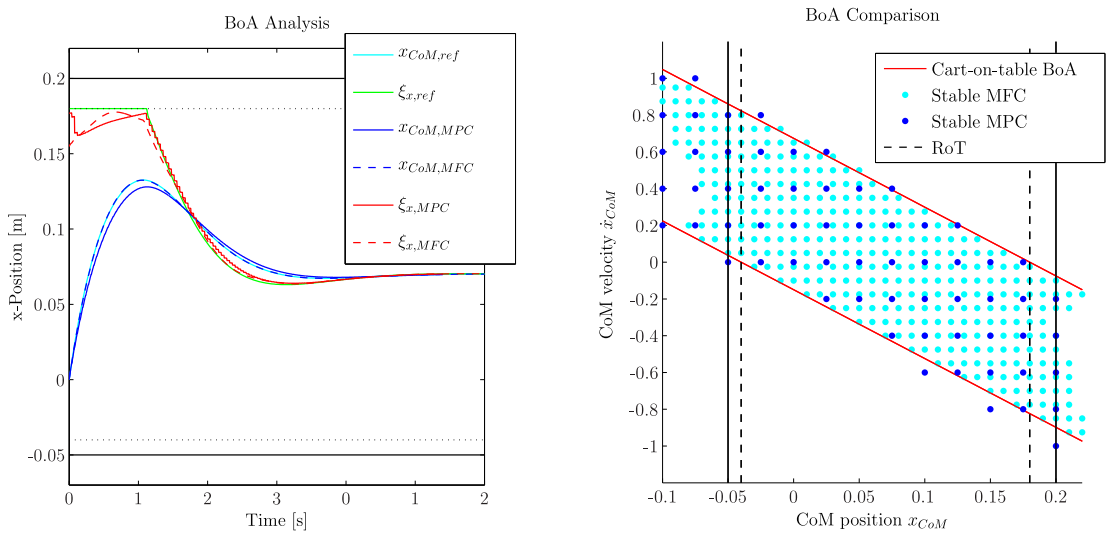

(a) Example for BoA derivation in the time-domain for an initial CoM state: $x_{CoM} = 0$ [m] and $\dot{x}_{CoM} = 0.65$ [m/s].

(b) Comparison of the cart-on-table basin of attraction with the one of the four-link CoM using both controllers, MFC and MPC.

Figure 3.7: Derivation and result of the bais of attraciton for the four-link basin of attraction.

achieved with both, MPC and MFC control. The cart-on-table model, used for trajectory generation, captures the relevant higher order dynamics of the controlled four-link model in combination with the CoM mapping. This function has been chosen such that the transition of the CoM leads to constant height and a total angular momentum that prevents ZMP peaks. The introduction of upper body counter rotation increases the just described effect on the angular momentum. By only considering the tracking quality, there is no reason to apply computationally expensive MPC. However, the following section about robustness of the system will highlight benefits of this optimization based method.

3.3.2 Robustness

To test the robustness of the system using MFC, MPC and ATR control, a horizontal impulse $\vec{p}$ is applied on the center of body (CoB) of the robot, in its energy optimized pose with a projected CoM position at the center of the RoT. The method of modeling contract forces for multi-body systems, suggested by P. Flores in [5] is used to calculate the distribution of the velocities induced by the impulse. A simplified derivation of the velocity distribution using this method can be found in Appendix C.

Applying an impulse on the CoB leads to instantaneous errors in the angular velocities. Considering the high gain feedback used for MFC, this causes high torques and can easily lead to an unstable system. By introducing ankle torque reduction, this problem is avoided. Allowing a zero ankle torque for a period of $t_{crit} = 0.03$ [s], the robustness with respect to impulsive disturbances is significantly increased. To see how well the suggested control approach works, the optimization based MPC controller has been developed. Figure 3.8a shows the comparison of the three described

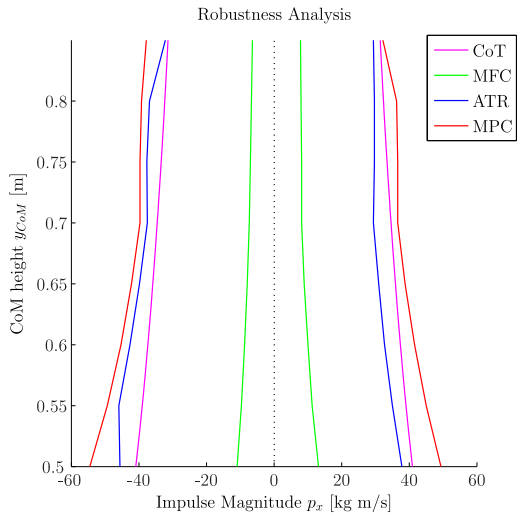

(a) Comparison of maximum applicable impulse as a function of the CoM height for MPC, MFC and ATR controlled system with the cart-on-table (CoT) robustness.

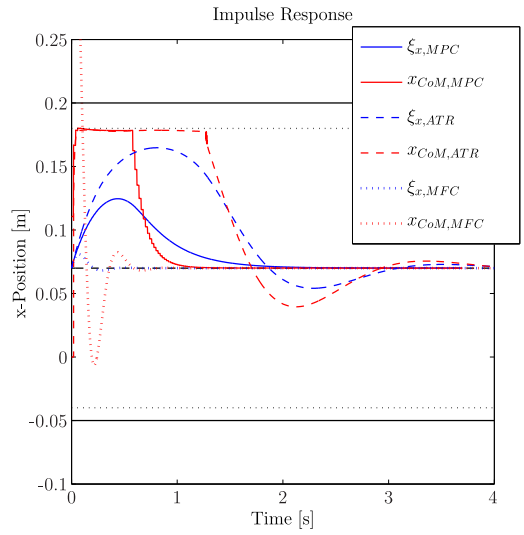

(b) Response of the four-link robot to an impulse of 35 [kg m/s] on the center of body under the influence of the three different controllers MPC, MFC and ATR.

Figure 3.8: Influence of chosen controller on the robustness of the system with respect to horizontal perturbations on the center of body.

control methods and points out the benefit of MPC: By running an online optimization and considering system dynamics, the overall robustness can be increased by a factor of up to 4.9 compared to model-based feedforward control. In comparison with the ATR controller, the use of MPC increases robustness by up to 20 %. The low robustness of the MFC is due to the fact, that this controller only considers errors in the joints and does not care about the overall system dynamics. By introducing ATR, this is partly taken care of by using ZMP limit torque control after all errors on non-ankle joints are driven to zero. However by using MPC, system dynamics that influence the ZMP are taken into account at all times by introducing constraints. Therefore, this method leads to high robustness.

The results of the robustness analysis is compared with the linear cart-on-table model from Chapter 2. As can be seen in Figure 3.8a, the optimization based approach for the four-link model leads to higher perturbation robustness than can be achieved with the cart-on-table model. This indicates, that the sophisticated used of additional links can increase the robustness of higher order systems. To underline the effect of the three controllers on the system, its impulse response is compared in Figure 3.8b. The MFC controller is not capable of handling the applied disturbance whereas the ankle torque reduction and model predictive controlled system maintains stability.

Considering the obtained results of the robustness and the good tracking behavior of the MPC, this control approach would be perfectly suited for the control of the four-link robot. However, the high computational effort that is required for the online optimization, makes the application on a real system questionable. A short comparison between of the MFC and MPC run-time needed for the reference tracking and disturbance rejection in Table 3.2 points that out. Time optimized

Problem-set	MFC [s]	MPC [s]
Reference tracking (Figure 3.5b)	0.45	10.3
Disturbance rejection (Figure 3.8b)	0.46	14.6

Table 3.2: Comparison of averaged run-time for MFC and MPC controlled four-link model for different problem-stes. Due to high computational demand, applicability of MPC is questionable.

controller design in for example C/C++ and an implementation on a physical system are necessary to determine its applicability.

Chapter 4

Conclusion and Outlook

4.1 Conclusion

The goal of this thesis was to examine the applicability of the preview control pattern generator suggested in [8] by using CoM tracking on a four-link inverted pendulum. This quantification has been done in the following steps.

First, the capabilities of the linear cart-on-table model used for the walking pattern generator, is exploited by introducing feedback control. The combined strategy of a LQR and ZMP limit force controller leads to a stable system with increased robustness. The herewith obtained explicit basin of attraction for the cart states indicates limitations on the robustness for the for the single support case of the model. Extending the simulations to the walking case, shows that at least the same robustness can be achieved by introducing acceleration and stopping steps, choosing a double support phase of 50 % and limiting the walking speed to 2.5 [km/h]. The question that arises from this linear model is how applicable the obtained results are to higher order models.

Therefore, in a second step, a nonlinear four-link inverted pendulum is introduced. The reference trajectories are followed by center of mass tracking. Creating a mapping function from the center of mass to relative joint angles and the application of model-based feedforward control with high feedback gains allows precise tracking while maintaining low computational effort. The stability critical zero moment point, which is not directly considered in the control law, follows the predicted ZMP from the trajectory generator closely. Even better, by sophisticated choice of the mapping function, stability critical peaks of the ZMP can be avoided and leads to the assumption that the cart-on-table model captures relevant dynamics of the higher order model. This observation is underlined by the fact that both model show the same basin of attraction within the region of trust. So by only considering tracking quality, the higher order model can be precisely controlled by model-based feedforward control with high feedback gains. However, these high gains introduce a small robustness of the system with respect to perturbations. By allowing an ankle torque reduction of perturbed systems this can be avoided and the robustness is increased by a factor of up to 4.5.

To compare the obtained tracking quality and robustness, a predictive controller that uses online optimization is introduced. Not surprising, this method increases the robustness by another 20 % compared to the ankle torque reduction controller and is capable of precisely tracking the center of mass. However, due to its high computational demand, its applicability on a physical system is questionable.

As a conclusion to the just provided summary the following important statements about the four-link inverted pendulum are pointed out

- Precise CoM tracking can be achieved by model-based feedforward control with high gain feedback on angular errors.
- This method is very sensitive to disturbances and an ankle torque reduction is introduced to increase robustness.
- By carefully choosing a function that maps the center of mass to relative joint angles, the relevant dynamics of the non-linear four-link inverted pendulum are captured by the cart-on-table model.
- The use of an online optimization based controller leads to the highest robustness in comparison with the model-based feedforward control and the ankle torque reduction approach. However its applicability is questionable due to the high computational demand.

4.2 Outlook

This thesis provides a simulation-based quantification of the walking control using preview control pattern generation and stabilizing feedback control applied to a four-link robot model in the sagittal plane. Future work based on the obtained results could include some of the following considerations.

- So far only the single support case of the four-link model has been examined. The next step would be to extend the four link robot by two additional legs. The obtained six link model could be used to examine the designed controllers for the walking case of the higher order robot model.
- The complete analysis in this thesis is done for the sagittal plane of the robot. This could be repeated for the robots frontal plane. Since the trajectory generation for both planes is decoupled, the procedure would be straight-forward.
- The four-link energy optimized reference pose, used for the mapping function is not optimized in regards to robustness. A pose optimization of the MFC controller could improve its robustness significantly. It easy to imagine that poses where horizontal impulses lead to a angular velocity distribution that cause small angular momentum around the ankle show higher robustness.
- The ankle torque reduction control method treats the four-link model as single link inverted pendulum. The introduction of a more sophisticated solution, that imitates the cart-on-table model with constant CoM height could improve its robustness capability.
- To get a better understanding of the applicability of the derived controllers, in particular the model predictive control approach, a validation on a simulator, such as the DARPA virtual robotics challenge simulator, is necessary.

Appendix A

Explicit LQR Basin of Attraction

From the equation of the cart-on-table ZMP controlled with LQR in equation (2.13), we know that the ZMP act like a sinusoid with exponential decay with different phase-shift and amplitude. We want to find the limits on the initial conditions x_0 and v_0 that still lead to a stable behaviour of the cart. In other words: For what initial conditions will the ZMP just reach the critical value $p_{x,lim}$ but not exceed it. As shown in Figure A.1a there are two different cases to consider.

1. The maximum ZMP occurs for a time $t > 0[s]$. In the phase plot, this case will appear as a stretched spiral and is from now on called the spiral limit function.

2. The ZMP reaches its maximum value at $t = 0[s]$. This case will lead to a linear dependency of the initial velocity and position. It is therefore called the linear limit function.

The idea for the spiral limit function is to consider the exponential growth of the ZMP taking the same sinusoid function with a phase shift such that the maximum admissible ZMP occurs at $t = 0[s]$ (see Figure A.1b). All points on that curve with the corresponding velocity must lie on the limit curve. Of course, with opposite signs of the velocity, since we are treating it as exponential growth instead of decay (Note: this is only used to determine the amplitudes and phase shifts for the limit functions). We start by stating the equation for the ZMP in a general way, with initial conditions $p_x(t = 0) = p_{x,lim}$ and $\dot{p}_x(t = 0) = 0$.

$$p_x = A\cos(\omega_d + \phi)e^{\zeta\omega_n t} \tag{A.1}$$

$$\dot{p_x} = 0 = -A\omega_d \sin(\omega_d t + \phi) + A\zeta\omega_n \cos(\omega_d t + \phi)e^{\zeta\omega_n t} \tag{A.2}$$

$$\therefore \quad \frac{\sin(\phi)}{\cos(\phi)} = \frac{\zeta\omega_n}{\omega_d} \rightarrow \phi = \arctan\left(\frac{\zeta\omega_n}{\omega_d}\right) \tag{A.3}$$

$$p_{x,lim} = A\cos(\phi) = A\left(\sqrt{1 + \left(\frac{\zeta\omega_n}{\omega_d}\right)^2}\right)^{-1} \tag{A.4}$$

$$\therefore \quad A = p_{x,lim}\sqrt{1 + \left(\frac{\zeta\omega_n}{\omega_d}\right)^2} \tag{A.5}$$

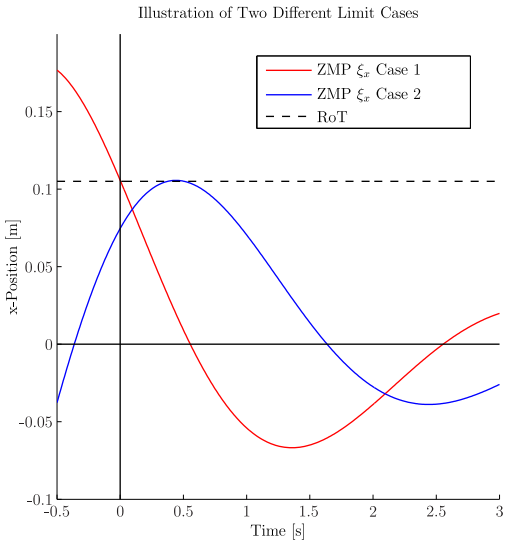

(a) Two different cases explained as sinusoid with exponential decay.

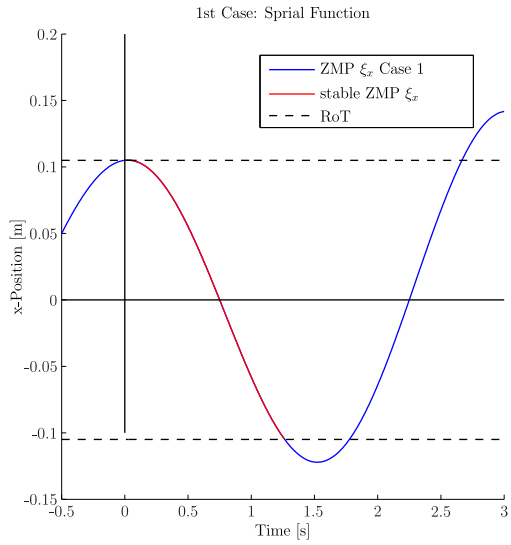

(b) Explanation of the set-up for the spiral limit function derivation.

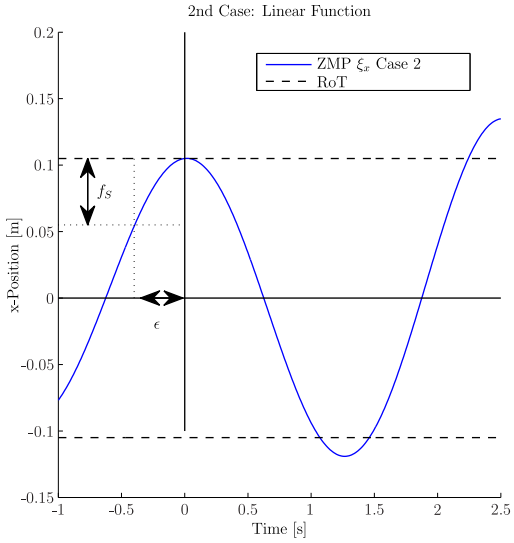

(c) Explanation of the set-up for the linear limit function derivation.

Figure A.1: Illustrations for the understanding of the explicit LQR RoA derivation.

To include the states of the cart-on-table model, its equation of motion is derived.

$$x = B\cos(\omega_d t + \eta)e^{\zeta\omega_n t} \tag{A.6}$$

$$\dot{x} = B\left[-\omega_d \sin(\omega_d t + \eta) + \zeta\omega_n \cos(\omega_d t + \eta)\right] e^{\zeta\omega_n t} \tag{A.7}$$

$$\ddot{x} = B\left[\left(-\omega_d^2 + (\zeta\omega_n)^2\right)\cos(\omega_d t + \eta) - 2\zeta\omega_n\omega_d \sin(\omega_d t + \eta)\right] e^{\zeta\omega_n t} \tag{A.8}$$

$$p_x = B\left[\underbrace{\left(1 - \frac{z_c}{g}\left(-\omega_d^2 + (\zeta\omega_n)^2\right)\right)}_{K_1}\cos(\omega_d t + \eta) + \underbrace{2\frac{z_c}{g}\zeta\omega_n\omega_d}_{K_2}\sin(\omega_d t + \eta)\right] e^{\zeta\omega_n t} \tag{A.9}$$

$$p_x = B\left[K_1\cos(\omega_d t + \eta) + K_2\sin(\omega_d t + \eta)\right] e^{\zeta\omega_n t} = A\cos(\omega_d + \phi)e^{\zeta\omega_n t} \tag{A.10}$$

at $t = 0$

$$\dot{p_x} = 0 = B\left[(K_1\zeta\omega_n + K_2\omega_d)\cos(\eta) + (K_2\zeta\omega_n - K_1\omega_d)\sin(\eta)\right] \tag{A.11}$$

$$\therefore \quad \eta = \arctan\left(\frac{-(K_1\zeta\omega_n + K_2\omega_d)}{(K_2\zeta\omega_n - K_1\omega_d)}\right) \tag{A.12}$$

$$B\left(K_1\cos(\eta) + K_2\sin(\eta)\right) = A\cos(\phi) \tag{A.13}$$

$$\therefore \quad B = \frac{A\cos(\phi)}{K_1\cos(\eta) + K_2\sin(\eta)} = \frac{p_{x,lim}}{K_1\cos(\eta) + K_2\sin(\eta)} \tag{A.14}$$

We now have an expression for the cart equation of motion in the limit case where the ZMP will just reach its limits.

For the linear limit function, the idea is to take the existing ZMP trajectory and find a range of phase shifts ϵ and amplitude scaling s such that the ZMP is $p_{x.lim}$ at $t = 0[s]$.

$$s = \frac{p_{x,lim}}{p_x} \tag{A.15}$$

$$p_x = B\left[K_1\cos(\omega_d t + \epsilon) + K_2\sin(\omega_d t + \epsilon)\right] e^{\zeta\omega_n t} \tag{A.16}$$

$$s = \frac{p_{x,lim}}{B\left(K_1\cos(\omega_d t + \epsilon) + K_2\sin(\omega_d t + \epsilon)\right) e^{\zeta\omega_n t}} \tag{A.17}$$

at $t = 0$

$$s = \frac{p_{x,lim}}{B\left(K_1\cos(\epsilon) + K_2\sin(\epsilon)\right)} \tag{A.18}$$

$$x(\epsilon, t = 0) = sB\cos(\epsilon) \tag{A.19}$$

$$\dot{x}(\epsilon, t = 0) = sB\left(-\omega_d\sin(\epsilon) + \omega_n\zeta\cos(\epsilon)\right) \tag{A.20}$$

$$x(\epsilon) = \frac{p_{x,lim}\cos(\epsilon)}{(K_1\cos(\epsilon) + K_2\sin(\epsilon))} \tag{A.21}$$

$$\dot{x}(\epsilon) = \frac{p_{x,lim}\left(-\omega_d\sin(\epsilon) + \omega_n\zeta\cos(\epsilon)\right)}{(K_1\cos(\epsilon) + K_2\sin(\epsilon))} \tag{A.22}$$

Equation (A.21) provides the following identities

$$\tan(\epsilon) = \frac{p_{x,lim} - K_1 x}{K_2 x} = F \tag{A.23}$$

$$\sin(\epsilon) = \frac{F}{\sqrt{1+F^2}} \tag{A.24}$$

$$\cos(\epsilon) = \frac{1}{\sqrt{1+F^2}} \tag{A.25}$$

Plugging those back into equations (A.22) leads to an explicit function of the limit on the region of attraction.

$$\dot{x} = \frac{\omega_n \zeta - \omega_d F}{K_1 + K_2 F} p_{x,lim} \tag{A.26}$$

$$= \frac{\omega_n \zeta - \omega_d \frac{p_{x,lim} - K_1 x}{K_2 x}}{K_1 + K_2 \frac{p_{x,lim} - K_1 x}{K_2 x}} p_{x,lim} \tag{A.27}$$

$$= \frac{p_{x,lim}\left(K_2 \omega_n \zeta x - \omega_d p_{x,lim} + \omega_d K_1 x\right)}{K_1 K_2 x + K_2 p_{x,lim} - K_1 K_2 x} \tag{A.28}$$

$$= x\left(\omega_n \zeta + \omega_d \frac{K1}{K2}\right) - \frac{\omega_d}{K_2} p_{x,lim} \tag{A.29}$$

The remaining problem is to get rid of the time dependency in the spiral limit function and how to merge it together with the linear limit functions. The trick is to introduce a change of variable and transform the equations into polar coordinates. We start by stating the equation of motion for the cart on the table. Note that this time we consider an exponential decay again.

$$x(t) = B\cos(\omega_d t + \eta) e^{-\zeta \omega_n t} \tag{A.30}$$

$$\dot{x}(t) = B\left(-\omega_d \sin(\omega_d t + \eta) - \omega_n \zeta \cos(\omega_d t + \eta)\right) e^{-\zeta \omega_n t} \tag{A.31}$$

The change of variables effects that x and $\dot{x}$ form a non-stretched spiral where the radius decays exponentially with increasing angles. This required that $\tilde{\dot{x}}(t)$ has the form of Equation A.32.

$$\tilde{\dot{x}}(t) = B e^{-\zeta \omega_n t} \sin(\omega_d t + \eta) \tag{A.32}$$

$$\rightarrow \quad \tilde{\dot{x}}(t) = \frac{1}{\omega_d}\left(-\dot{x}(t) + \zeta \omega_n x\right) \tag{A.33}$$

All the so far obtained results are now transformed into polar coordinates, starting with the spiral limit function.

$$R = \sqrt{x^2 + \tilde{\dot{x}}^2} = B e^{-\zeta \omega_n t} \tag{A.34}$$

$$\theta = \arctan\left(\frac{\tilde{\dot{x}}}{x}\right) = \omega_d t + \eta \quad \rightarrow \quad t = \frac{\theta - n}{\omega_d} \tag{A.35}$$

$$R_{spiral}(\theta) = B e^{-\zeta \frac{\omega_n}{\omega_d}(\theta - \eta)} \tag{A.36}$$

The second part builds the linear function form equation (A.29):

$$\dot{x} = x\left(\omega_n\zeta + \omega_d\frac{K1}{K2}\right) - \frac{\omega_d}{K_2}p_{x,lim} \tag{A.37}$$

$$\tilde{\dot{x}} = -x\frac{K_1}{K_2} + \frac{p_{x,lim}}{K_2} = ax + b \tag{A.38}$$

$$R = \sqrt{x^2 + \tilde{\dot{x}}^2} = \sqrt{x^2(1+a^2) + 2abx + b^2} \tag{A.39}$$

$$\theta = \arctan\left(\frac{\tilde{\dot{x}}}{x}\right) \quad \rightarrow \quad \tan(\theta) = a + \frac{b}{x} \tag{A.40}$$

$$\rightarrow \quad x = \frac{b}{\tan(\theta) - a} \tag{A.41}$$

$$R_{linear}(\theta) = \sqrt{\frac{b^2(1+a^2)}{(\tan(\theta) - a^2)^2} + \frac{2ab^2}{(\tan(\theta) - a^2)} + b^2} \tag{A.42}$$

The only missing part are the angles θ_1 and θ_2 at which the two limits (linear and spiral) cross and where we switch from one limit to the other. From equation (A.30) we know the solution at $t = 0$:

$$x(t=0) = B\cos\eta \tag{A.43}$$

$$\tilde{\dot{x}}(t=0) = B\sin\eta \tag{A.44}$$

$$\tan(\theta_1) = \frac{\tilde{\dot{x}}}{x} = \tan(\eta) \quad \rightarrow \quad \theta_1 = \eta \tag{A.45}$$

The solution for θ_2 is not easy to find analytically but can be determined numerically. Another way is to state the angles at which one of the two solutions has to be applied.

$$\text{linear limit function:} \quad -\pi \leq \theta \leq \theta_1 - \pi \tag{A.46}$$

$$\text{min(linear,spiral):} \quad \theta_1 - \pi < \theta \leq 0 \tag{A.47}$$

To summarize: After the modifying of the current state of the cart-on-table (change of variables and transformation into polar coordinates), the RoA can be stated as follows. Figure A.2 shows the derivation of the RoA in plots.

$$\theta_{act} = \arctan\left(\frac{\frac{1}{\omega_d}(-\dot{x} + \zeta\omega_n x)}{x}\right) \quad \text{and} \quad R_{act} = \sqrt{x^2 + \left(\frac{1}{\omega_d}(-\dot{x} + \zeta\omega_n x)\right)^2} \tag{A.48}$$

$$R_{act} < R_{lin}(\theta_{act}) \quad \text{for} \quad \pi \leq \theta_{act} \leq \eta - \pi \tag{A.49}$$

$$R_{act} < \min(R_{lin(\theta_{act})}, R_{sp}(\theta_{act})) \quad \text{for} \quad \eta - \pi \leq \theta_{act} \leq 0 \tag{A.50}$$

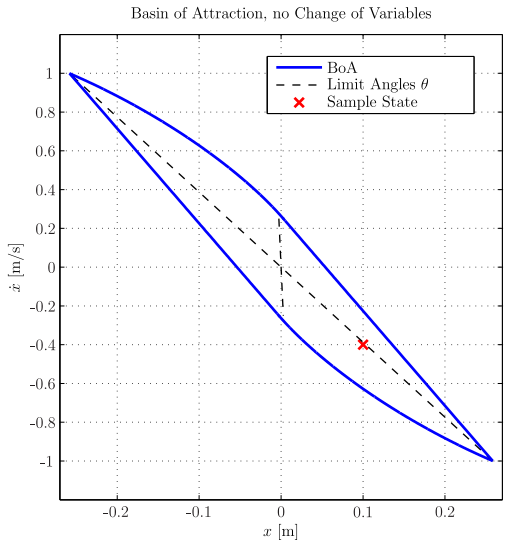

(a) RoA in the cartesian coodinate system with a squeezed spiral limit function.

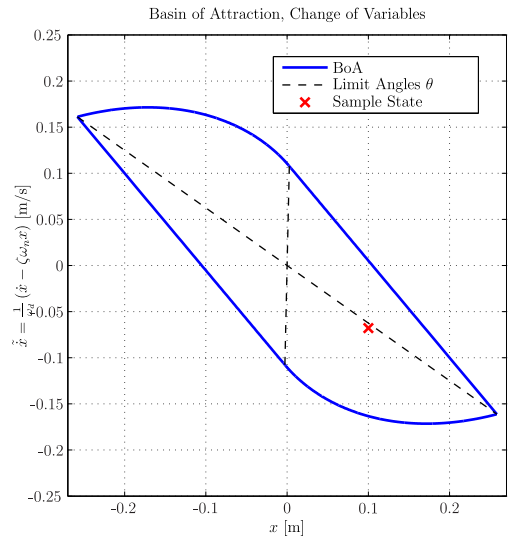

(b) Application of the change of variables which leads to a non-squeezed spiral limit function.

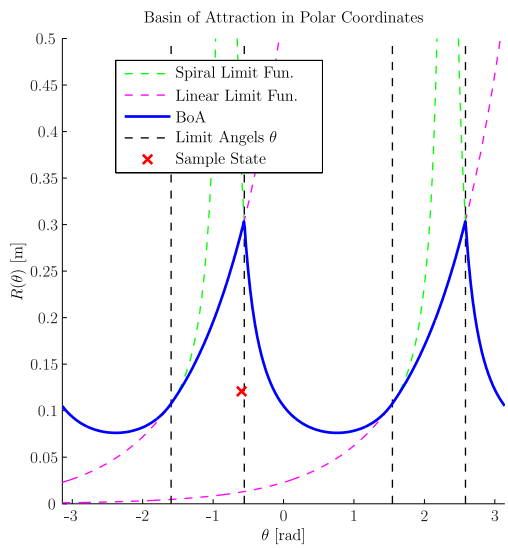

(c) Explicit solution of the ROA in the polar coordinate system. Note, that the RoA is periodic with with respect to the angle θ.

Figure A.2: Illustration of the three steps of the LQR RoA derivation.

Appendix B

Four-Link Model Equation of Motion

For the derivation of the four-link dynamics the Lagrangian formalism is used. The relative angles θ_i of the four links are used as generalized coordinates $\vec{q} = [\theta_1 \theta_2 \theta_3 \theta_4]^\top$. Additionally, for simplicity, we introduce the absolute angles ϕ_i of link i which can be obtained by simply adding up all previous relative angles

$$\phi_i = \sum_{k=1}^{i} \theta_k \tag{B.1}$$

The Lagrangian is defined as

$$L = T - V \tag{B.2}$$

where T is the kinetic and V the potential energy. The energy of each link can be obtained separately

$$T_i = \frac{1}{2} m_i \vec{v}_i^\top \vec{v}_i + \frac{1}{2} J_i \vec{\Omega}_i^\top \vec{\Omega}_i \tag{B.3}$$

$$V_i = -m_i \vec{g}^\top \vec{r}_{0i} \quad \text{with} \quad \vec{g}^\top = [0, -g, 0] \tag{B.4}$$

where $\vec{v}_i$ is the velocity of the CoM of each link and $\vec{\Omega}_i$ the angular velocity around it. Summing them up provides the total kinetic and potential energy

$$T = \sum_{i=1}^{4} T_i \quad \text{and} \quad V = \sum_{i=1}^{4} V_i \tag{B.5}$$

We start by stating the coordinate vector of the CoM for each link i

$$\vec{r}_{01} = \begin{pmatrix} -lc_1 \sin(\phi_1) \\ lc_1 \cos(\phi_1) \\ 0 \end{pmatrix} \tag{B.6}$$

$$\vec{r}_{02} = \begin{pmatrix} -L_1 \sin(\phi_1) - lc_2 \sin(\phi_2) \\ L_1 \cos(\phi_1) + lc_2 \sin(\phi_2) \\ 0 \end{pmatrix} \tag{B.7}$$

$$\vec{r}_{03} = \begin{pmatrix} -L_1 \sin(\phi_1) - L_2 \sin(\phi_2) - lc_3 \sin(\phi_3) \\ L_1 \cos(\phi_1) + L_2 \sin(\phi_2) + lc_3 \sin(\phi_3) \\ 0 \end{pmatrix} \tag{B.8}$$

$$\vec{r}_{04} = \begin{pmatrix} -L_1 \sin(\phi_1) - L_2 \sin(\phi_2) - L_3 \sin(\phi_3) - lc_4 \sin(\phi_4) \\ L_1 \cos(\phi_1) + L_2 \sin(\phi_2) + L_3 \sin(\phi_3) + lc_4 \sin(\phi_4) \\ 0 \end{pmatrix} \tag{B.9}$$

The required velocities are obtained through derivation of the CoM of each link w.r.t. time

$$\vec{v}_1 = \begin{pmatrix} -lc_1 \dot{\phi}_1 \cos(\phi_1) \\ -lc_1 \dot{\phi}_1 \sin(\phi_1) \\ 0 \end{pmatrix} \tag{B.10}$$

$$\vec{v}_2 = \begin{pmatrix} -L_1 \dot{\phi}_1 \cos(\phi_1) - lc_2 \dot{\phi}_2 \cos(\phi_2) \\ -L_1 \dot{\phi}_1 \sin(\phi_1) - lc_2 \dot{\phi}_2 \sin(\phi_2) \\ 0 \end{pmatrix} \tag{B.11}$$

$$\vec{v}_3 = \begin{pmatrix} -L_1 \dot{\phi}_1 \cos(\phi_1) - L_2 \dot{\phi}_2 \cos(\phi_2) - lc_3 \dot{\phi}_3 \cos(\phi_3) \\ -L_1 \dot{\phi}_1 \sin(\phi_1) - L_2 \dot{\phi}_2 \sin(\phi_2) - lc_3 \dot{\phi}_3 \sin(\phi_3) \\ 0 \end{pmatrix} \tag{B.12}$$

$$\vec{v}_4 = \begin{pmatrix} -L_1 \dot{\phi}_1 \cos(\phi_1) - L_2 \dot{\phi}_2 \cos(\phi_2) - L_3 \dot{\phi}_3 \cos(\phi_3) - lc_4 \dot{\phi}_4 \cos(\phi_4) \\ -L_1 \dot{\phi}_1 \sin(\phi_1) - L_2 \dot{\phi}_2 \sin(\phi_2) - L_3 \dot{\phi}_3 \sin(\phi_3) - lc_4 \dot{\phi}_4 \sin(\phi_4) \\ 0 \end{pmatrix} \tag{B.13}$$

$$\vec{\Omega}_i = \begin{pmatrix} 0 \\ 0 \\ \dot{\phi}_i \end{pmatrix} \quad \text{for} \quad i = 1 \ldots 4 \tag{B.14}$$

The just derived vectors are used for the calculation of the kinetic T and potential energy V. Through the Lagrangian L, the equation of motion can be derived by applying

$$\frac{d}{dt} \frac{\partial L}{\partial \dot{\vec{q}}} - \frac{\partial L}{\partial \vec{q}} = 0 \tag{B.15}$$

Remodeling the result leads to the equation of motion in the form of

$$M(\vec{q})\ddot{\vec{q}} + H(\dot{\vec{q}}, \vec{q}) = \vec{\tau} \tag{B.16}$$

where $M(\vec{q}) \in \mathbb{R}^{4\times4}$ is the mass matrix, $H(\dot{\vec{q}}, \vec{q}) \in \mathbb{R}^{4\times1}$ contains the gyroscopic and Coriolis forces and $\tau = [\tau_1 \tau_2 \tau_3 \tau_4]^\top \in \mathbb{R}^{4\times1}$ are the torques in each joint.

Appendix C

Impulse on Four-Link Model

The calculation of the angular velocity distribution after an impulse on the four-link robot model is based on P. Flores paper [5]. This method takes into account the actual state of the robot as well as the acting torques.This chapter provides a summary of the paper and the application on the four-link.

First, the general equation of motion for a multi-body system with generalized coordinates q, which are the relative angles in the four-link case, can be written as

$$M\dot{u} - h = 0 \tag{C.1}$$

$$\dot{q} = u \quad \forall t \tag{C.2}$$

with M being the mass matrix, h the vector of all external and gyroscopic forces and u the derivative of the generalized coordinates. Since an impulse can be interpreted as a force acting on the robot for a very short period of time, contact forces in normal and tangential directions are added.

$$M\dot{u} - h - W_N\lambda_N - W_T\lambda_T \tag{C.3}$$

$$\dot{q} = u \quad \forall t \tag{C.4}$$

W_N and W_T gather the generalized normal and tangential force directions w_{Ni} and w_{Ti} of forces with magnitudes captured in λ_N and λ_T respectively. Multiplying equation C.4 with the Lebesque measure dt and considering that the force acting on the system over a very short period of time can be written as the derivative of impulse P, leads to

$$Mdu - hdt - W_N dP_N - W_T dP_T = 0 \tag{C.5}$$

This equation can be solved using Moreaus time-stepping method. First time discretization (integration of C.5 over a small Δt) indexing initial and end time with A and E, leads to the following

approximations:

$$\int_{\Delta t} M du \approx M_M \Delta u, \quad M_M = M(q_M, t_M) \tag{C.6}$$

$$\int_{\Delta t} h dt \approx h_M \Delta t u, \quad h_M = h(q_M, t_M) \tag{C.7}$$

$$\int_{\Delta t} W_N dP_N \approx W_{NM} P_N, \quad W_{NM} = W_N(q_M, t_M) \tag{C.8}$$

$$\int_{\Delta t} W_T dP_T \approx W_{TM} P_T, \quad W_{TM} = W_T(q_M, t_M) \tag{C.9}$$

$$\tag{C.10}$$

where $q_M = q_A + \frac{1}{2} u_a \Delta t$ and $t_M = t_A + \frac{1}{2}\Delta t$. Plugging the above back into equation C.5 completes the derivation of the influence of an impulse on a multi-body system.

$$M_M(u_E - u_A) - h_M \Delta t - W_{NM} P_N - W_{TM} P_T = 0 \tag{C.11}$$

This equation can be solved for the velocity distribution of the four-link model after an impulse acts on the system.

$$u_E = u_A + M_M^{-1}(h_M \Delta t + W_{NM} P_N + W_{TM} P_T) \tag{C.12}$$

It is assumed that the robot experiences a horizontal impulse in its steady state (all initial velocities are zero) on the center of body (CoB). First the generalized normal and tangential directions of the forces are derived. We start by staging the Jacobian at the CoB.

$$J_{c3} = \begin{pmatrix} -L_1 \cos(\phi_1) - L_2 \cos(\phi_2) - l_{c3} \cos(\phi_3) & -L_2 \cos(\phi_2) - l_{c3} \cos(\phi_3) & -l_{c3} \cos(\phi_3) & 0 \\ -L_1 \sin(\phi_1) - L_2 \sin(\phi_2) - l_{c3} \sin(phi_3) & -L_2 \sin(\phi_2) - l_{c3} \sin(\phi_3) & -l_{c3} \sin(\phi_3) & 0 \\ 0 & 0 & 0 & 0 \end{pmatrix} \tag{C.13}$$

where ϕ_1, ϕ_2, ϕ_3 and ϕ_4 are the absolute angles of the four link with respect to the y-axis. Multiplying the transposed Jacobian with the unit vector of the in the tangential and normal direction leads to the generalized direction matrices W_T and W_N.

$$n_T = \begin{pmatrix} -\sin(\phi_3) \\ \cos(\phi_3) \\ 0 \end{pmatrix} \quad \text{and} \quad n_N = \begin{pmatrix} \cos(\phi_3) \\ \sin(\phi_3) \\ 0 \end{pmatrix} \tag{C.14}$$

$$W_N = J_{c3}^T n_N = \begin{pmatrix} -L_1 \cos(\phi_1 + \phi_3) - L_2 \cos(\phi_3) \\ -L_2 \cos(\phi_3) \\ -l_{c3} \\ 0 \end{pmatrix} \tag{C.15}$$

$$W_T = J_{c3}^T n_T = \begin{pmatrix} L_1 \sin(\phi_1 + \phi_3) + L_2 \sin(\phi_3) \\ L_2 \cos(\phi_3) \\ 0 \\ 0 \end{pmatrix} \tag{C.16}$$

The remaining P_N and P_T are the normal and tangential components of the horizontal impulse with respect to the body-link of the four-link model.

$$p = \begin{pmatrix} p_x \\ 0 \\ 0 \end{pmatrix} \tag{C.17}$$

$$\rightarrow P_N = p_x \cos(\phi_3) \quad \text{and} \quad P_T = -p_x \sin(\phi_3) \tag{C.18}$$

We have now everything in place to solve for the velocity distribution of the angles after an impulse on the system by simply plug the relevant parameters into equation (C.12).

Bibliography

[1] K Akachi, K Kaneko, N Kanehira, S Ota, G Miyamori, M Hirata, S Kajita, and F Kanehiro. Development of humanoid robot HRP-3P. In *Humanoid Robots, 2005 5th IEEE-RAS International Conference on*, pages 50–55, 2005.

[2] G Bessonnet, S Chesse, and P Sardain. Optimal gait synthesis of a seven-link planar biped. *The International Journal of Robotics Research*, 2004.

[3] T Buschmann, S Lohmeier, H Ulbrich, and F Pfeiffer. Optimization based gait pattern generation for a biped robot. In *Humanoid Robots, 2005 5th IEEE-RAS International Conference on*, pages 98–103, 2005.

[4] DARPA. DARPA Robotics Challenge Homepage. In *http://www.theroboticschallenge.org/*, April 2013.

[5] P Flores, R Leine, and C Glocker. Modeling and analysis of planar rigid multibody systems with translational clearance joints based on the non-smooth dynamics approach. *Multibody System Dynamics*, 2010.

[6] M Giftthaler and K Byl. Increased Robustness of Humanoid Standing Balance in the Sagittal Plane through Adaptive Joint Torque Reduction. *Intelligent Robots and Systems, 2007. IROS 2013. IEEE/RSJ International Conference on*, 2013.

[7] M Hirose and K Ogawa. Honda humanoid robots development. *Philosophical Transactions of the Royal Society A*, 365(1850):11–19, January 2007.

[8] S Kajita, F Kanehiro, K Kaneko, K Fujiwara, K Harada, K Yokoi, and H Hirukawa. Biped walking pattern generation by using preview control of zero-moment point. In *Robotics and Automation, 2003. Proceedings. ICRA '03. IEEE International Conference on*, pages 1620–1626, 2003.

[9] S Kajita, F Kanehiro, K Kaneko, K Yokoi, and H Hirukawa. The 3D linear inverted pendulum mode: a simple modeling for a biped walking pattern generation. In *Intelligent Robots and Systems, 2001. Proceedings. 2001 IEEE/RSJ International Conference on*, pages 239–246, 2001.

[10] S Kajita, M Morisawa, K Miura, S Nakaoka, K Harada, K Kaneko, F Kanehiro, and K Yokoi. Biped walking stabilization based on linear inverted pendulum tracking. In *Intelligent Robots and Systems (IROS), 2010 IEEE/RSJ International Conference on*, pages 4489–4496, 2010.

[11] K Kaneko, K Harada, F Kanehiro, G Miyamori, and K Akachi. Humanoid robot HRP-3. In *Intelligent Robots and Systems, 2008. IROS 2008. IEEE/RSJ International Conference on*, pages 2471–2478. IEEE, 2008.

[12] T Katayama, T Ohki, T Inoue, and T Kato. Design of an optimal controller for a discrete-time system subject to previewable demand. *International Journal of Control*, 1985.

[13] K Nagasaka, H Inoue, and M Inaba. Dynamic walking pattern generation for a humanoid robot based on optimal gradient method. In *Systems, Man, and Cybernetics, 1999. IEEE SMC '99 Conference Proceedings. 1999 IEEE International Conference on*, pages 908–913, 1999.

[14] Gabe Nelson, Aaron Saunders, B Swilling, J Bondaryk, D Billings, C Lee, R Playter, and M Raibert. Petman: A humanoid robot for testing chemical protective clothing. *Journal of the Robotics Society of Japan*, 30:372–377, 2012.

[15] Open Source Robotics Foundation. Darpa Robotics Challenge - Gazebo Wiki. In *http://gazebosim.org/wiki/DRC/*, April 2013.

[16] Y Sakagami, R Watanabe, C Aoyama, S Matsunaga, N Higaki, and K Fujimura. The intelligent ASIMO: system overview and integration. In *Intelligent Robots and Systems, 2002. IEEE/RSJ International Conference on*, pages 2478–2483. IEEE, 2002.

[17] B J Stephens and C G Atkeson. Push Recovery by stepping for humanoid robots with force controlled joints. In *Humanoid Robots (Humanoids), 2010 10th IEEE-RAS International Conference on*, pages 52–59. IEEE, 2010.

[18] T Sugihara, Y Nakamura, and H Inoue. Real-time humanoid motion generation through ZMP manipulation based on inverted pendulum control. In *Robotics and Automation, 2002. Proceedings. ICRA '02. IEEE International Conference on*, pages 1404–1409, 2002.

[19] M Vukobratović and B Borovac. Zero-moment point—thirty five years of its life. *International Journal of Humanoid Robotics*, 1(1):157–173, 2004.